Received: 28 November 2022 | Revised: 22 April 2023 | Accepted: 2 May 2023

DOI: 10.1111/jmg.12736

ORIGINAL ARTICLE

Journal of METAMORPHIC GEOLOGY WILEY

Growth of kyanite and Fe-Mg chloritoid in Fe_2O_3-rich high-pressure–low-temperature metapelites and metapsammites: A case study from the Massa Unit (Alpi Apuane, Italy)

Samuele Papeschi[1] | **Federico Rossetti**[2] | **Jesse B. Walters**[3]

[1]Japan Agency for Marine – Earth Science and Technology (JAMSTEC), Kochi Institute for Core Sample Research (X-Star), Nankoku, Japan

[2]Dipartimento di Scienze, Università Roma Tre, Rome, Italy

[3]Institut für Geowissenschaften, Goethe Universität, Frankfurt am Main, Germany

Correspondence
Jesse B. Walters, Institut für Geowissenschaften, Goethe Universität, Frankfurt am Main, Germany.
Email: walters@em.uni-frankfurt.de

Handling Editor: Prof. Clare Warren

Abstract

Chloritoid and kyanite coexist in metapelites from the high-pressure/low-temperature Massa Unit in the Alpi Apuane metamorphic complex (Northern Apennines, Italy). The composition of chloritoid is extremely variable throughout the Massa Unit. Fe-chloritoid occurs in association with hematite-free, graphite-bearing schists, whereas strongly zoned Fe-Mg chloritoid is found with hematite and kyanite. We investigated the effect of different bulk Fe_2O_3 contents in controlling chloritoid composition through phase equilibria modelling of four selected samples, representative of the different chloritoid-bearing parageneses found in the Massa Unit. The ferric iron content, measured through wet chemical titration, ranges from 0 (graphite-chloritoid schist) to 73% of the total iron (hematite-chloritoid schist). We show that Mg-rich chloritoid compositions and stability of kyanite at greenschist to blueschist facies conditions can be reproduced in the $MnO–Na_2O–K_2O–FeO–MgO–Al_2O_3–SiO_2–H_2O–TiO_2–O$ (MnNKFMASHTO) chemical system only considering the presence of significant amounts of ferric iron as part of the bulk composition. The stabilization of kyanite at lower grade is directly linked to the presence of Fe_2O_3, which renders the reactive bulk rock composition effectively enriched in Al_2O_3 with respect to Fe and Mg. We also document that high Fe_2O_3 contents exacerbate the effect of chloritoid fractionation, producing strongly zoned Fe-Mg-chloritoid grains. Finally, the P–T modelling of the Massa Units performed in this study allows, for the first time, the recognition of a two-stage evolution at peak conditions, with an earlier pressure peak (1.2–1.3 GPa at 350–400°C), and a later thermal peak (0.7–1.1 GPa at 440–480°C), compatible with subduction, underthrusting and exhumation of the Adria continental margin during growth of the Northern Apennine orogenic wedge.

KEYWORDS
chloritoid, ferric iron, kyanite, Northern Apennines, phase equilibria modelling

1 | INTRODUCTION

Chloritoid is a common metamorphic mineral in pelitic schists formed at low-grade conditions, both under high-pressure–low-temperature (HP–LT) subduction-zone and Barrovian metamorphic conditions (Albee, 1972; Chopin et al., 1992; Chopin & Schreyer, 1983; Ganguly, 1969; Hoschek, 1969; Nerone et al., 2023; Zhou et al., 1994). Experimental studies and investigation of natural chloritoid-bearing rocks have shown that the composition of chloritoid becomes increasingly Mg-rich during prograde metamorphism in the presence of other Fe-, Mg-bearing phases, such as chlorite, phengite, and carpholite (Ashworth & Evirgen, 1984; Chopin, 1983; Simon et al., 1997; Theye et al., 1992; Vidal et al., 1994). The variation of X_{Mg} (=Mg apfu/[Mg apfu + Fe apfu]; apfu = atoms per formula unit) in chloritoid has been used to calibrate the chlorite–chloritoid geothermometer (Vidal et al., 1999) and applied qualitatively to low-grade metamorphic terranes, such as those of the Alpine circum-Mediterranean belts, to estimate the climax of orogenic metamorphism (Ashworth & Evirgen, 1984; Azañón & Goffé, 1997; Bouybaouene et al., 1995; Giorgetti et al., 1998; Jolivet et al., 1998; Vidal et al., 1999; Franceschelli & Memmi, 1999; Molli, Giorgetti, & Meccheri, 2000; Balen et al., 2013). However, results of several studies have shown the strong dependence of the X_{Mg} in chloritoid on the bulk Fe_2O_3 content of the rock, the partitioning of Fe^{3+} in silicates, and the coexistence of chloritoid with other Fe-Mg phases (Forshaw & Pattison, 2021; Lo Pò & Braga, 2014; López-Carmona et al., 2013; Pourteau et al., 2014). Pourteau et al. (2014) documented that the progressive growth of chloritoid consuming Fe-Mg phases such as carpholite results in strongly zoned chloritoid grains, with high X_{Mg} contents (up to 0.25–0.30) at relatively low temperature conditions (T ∼350–400°C). Lo Pò and Braga (2014) documented chloritoid with $X_{Mg} = 0.16$ stabilized at T ∼475°C in Fe_2O_3-bearing bulk-rock compositions, 75°C lower than the Fe^{3+}-free case. Similarly, both Lo Pò and Braga (2014) and Papeschi, Pontesilli, et al. (2022) reported P–T-X pseudosections where the predicted appearance of kyanite in the metamorphic assemblage of Al-rich metapelites appears to be linked exclusively to high-Fe_2O_3 contents, highlighting the potential use of chloritoid-kyanite-bearing assemblages as tracers of the P–T evolution and the state of oxidation of iron during metamorphism. However, the stability of kyanite or other Al-silicates as controlled by the ferric iron content, while possible theoretically, has never been documented in low-grade metamorphic rocks.

In this study, we investigate the metamorphic evolution of the HP–LT Massa Unit of the Alpi Apuane (Northern Apennines, Italy; Figure 1), where kyanite coexists with high-X_{Mg} chloritoid as part of the peak metamorphic assemblage (Franceschelli & Memmi, 1999). We show that, even though fractionated growth of chloritoid surely played a role in the development of zoned chloritoid grains, elevated X_{Mg} contents are detected only in chloritoid from hematite-bearing schists (with high Fe_2O_3 contents) and not in hematite-free graphite-bearing rocks. Furthermore, we document the appearance of kyanite as part of the assemblage due to the presence of elevated Fe_2O_3 in the bulk composition. Our results (1) highlight the importance of considering the Fe^{3+} content when modelling low-grade HP metamorphism in metapelites and (2) provide new constraints on the peak P–T conditions reached by subducted continental units during the tectono–metamorphic evolution of the Northern Apennine orogenic wedge.

2 | GEOLOGICAL BACKGROUND

The Northern Apennines are a NE-verging orogen that developed above the retreating Adria plate, which was involved in a W -dipping subduction beneath the European plate, at least from Eocene–Oligocene times (e.g., Boccaletti et al., 1971; Elter, 1975; Kligfield, 1979; Coward & Dietrich, 1989; Faccenna et al., 2001; Carminati et al., 2012; Molli, 2008; Vignaroli et al., 2008; Bonini et al., 2014; Molli, Carlini, et al., 2018; Papeschi, Vannucchi, et al., 2022; Rossetti et al., 2023) (Figure 1). The subduction of the continental margin of Adria produced continent-derived greenschist/blueschist facies units, collectively known as the Tuscan Metamorphic Units (TMUs), which crop out in tectonic windows at the base of the orogenic edifice, under a pile of non-metamorphic to anchizone (subgreenschist) facies nappes (ocean-derived Ligurian Units and continent-derived-Tuscan Nappe). The TMUs largely consist of metasedimentary rocks (metapelites, metapsammites and metacarbonates), locally containing lenses of metabasites. Their protoliths comprise a Palaeozoic (Variscan) basement, a Permian–Triassic continental cover, discontinuous Mesozoic passive margin successions, and local Cenozoic foredeep deposits (Cassinis et al., 2018; Conti et al., 2020; Patacca et al., 2013). The HP–LT metamorphic event is attested by (Fe, Mg)-chloritoid ± carpholite-bearing assemblages in metapelites/metapsammites, which record metamorphic pressures of ∼0.8–1.8 GPa at T = 300–500°C (Brogi & Giorgetti, 2012; Franceschelli et al., 1986, 1996, 1997; Franceschelli & Memmi, 1999; Theye et al., 1997; Giorgetti et al., 1998; Giuntoli & Viola, 2021; Jolivet et al., 1998; Lo Pò & Braga, 2014; Molli, Giorgetti, & Meccheri, 2000; Papeschi et al., 2020;

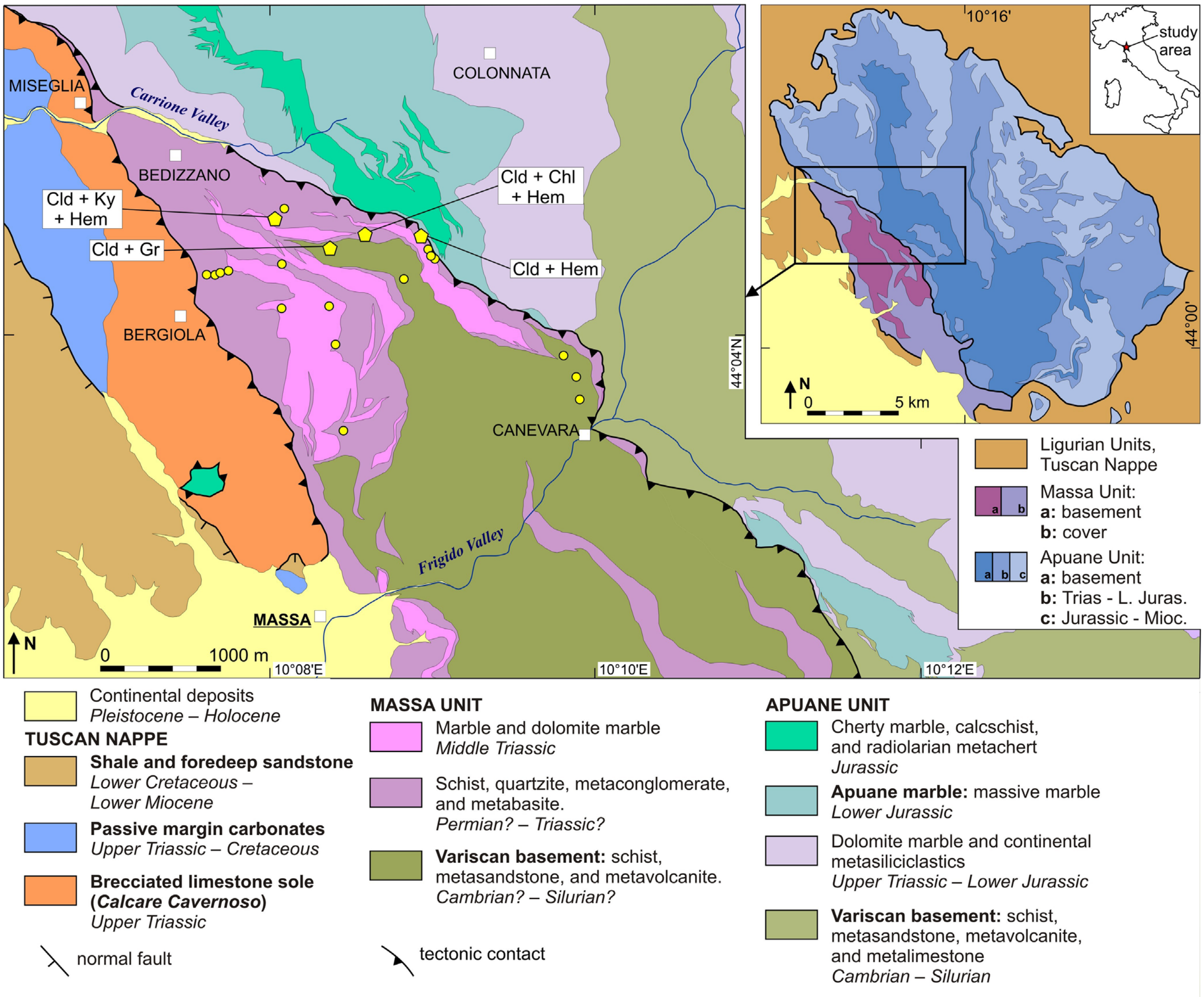

FIGURE 1 Geological sketch map of the Massa Unit and inset showing the location of the study area in the Alpi Apuane metamorphic complex. The map is based on Conti et al. (2019) and has been modified based on field work carried out in the present work. Yellow circles: samples for petrographic investigation. Yellow pentagons: samples for mineral chemistry, bulk rock chemistry, and phase equilibrium modelling.

Papeschi, Pontesilli, et al., 2022; Rossetti et al., 1999, 2002). The age of subduction zone metamorphism in the inner Northern Apennines is still poorly constrained due to the intense post-peak greenschist facies retrograde metamorphism. Available age constrains are based mainly on $^{40}Ar/^{39}Ar$ white mica geochronology, which yielded ages spanning from ~15 to 27 Ma (Bianco et al., 2019; Brunet et al., 2000; Di Vincenzo et al., 2022; Kligfield et al., 1986; Rossetti et al., 2001; Ryan et al., 2021).

The Alpi Apuane metamorphic complex forms the northernmost and most extensively investigated outcrop of the TMUs (Figure 1) and its tectono-metamorphic evolution has been widely used to constrain the syn- and post-orogenic evolution of the entire Northern Apennines orogen (Carmignani et al., 2001, 2004; Carmignani & Kligfield, 1990; Carosi et al., 2004; Di Vincenzo et al., 2022; Fellin et al., 2007; Jolivet et al., 1998; Molli et al., 2002; Molli, Carlini, et al., 2018). The structure of the Alpi Apuane consists of a dome of metamorphic rocks cropping out in a tectonic window below the very low-grade Tuscan Nappe and Ligurian Units (Figure 1). Two main tectonic units are exposed in this complex: the lower-grade Apuane Unit to the east—at the base of the nappe stack—and the higher-grade Massa Unit to the west, which tectonically overlies the Apuane Unit (Figure 1). The Massa Unit preserves the only known occurrence of the chloritoid + kyanite paragenesis in the

Northern Apennines and, for this reason, it has been considered the unit with the highest metamorphic grade among the TMUs (Franceschelli et al., 1986). Both the Apuane Unit and Massa Unit are characterized by a comparable Palaeozoic basement comprising schists, metapsammites, quartzites, and metavolcanites, with rare marbles. This basement is overlain by a mainly carbonatic Mesozoic–Cenozoic succession in the Apuane Unit and by a thick Permian–Triassic succession of metasedimentary rocks (schist, metapsammite, metaconglomerate, metabreccias, and marbles) in the Massa Unit (Conti et al., 1993, 2019; Patacca et al., 2011). The overlying Tuscan Nappe (Figure 1) consists of Triassic–Palaeogene carbonate passive margin sequences and Oligocene foredeep deposits (Macigno Fm.), detached from their original basement (Baldacci et al., 1967; Ciarapica & Passeri, 1994; Ricci Lucchi, 1986). The base of the Tuscan Nappe is represented by the *Calcare Cavernoso* Fm., a cataclastic horizon derived from Triassic evaporite sequences that marks the tectonic boundary between the Tuscan Nappe above the underlying Apuane and Massa units below.

The peak metamorphic temperatures reached by the Tuscan Nappe are estimated to be in the ~230°C to ~270°C range, based on Raman Spectroscopy on Carbonaceous Material (RSCM) thermometry data (Molli, Brovarone, et al., 2018), and ~260–280°C, based on fluid inclusions in syntectonic veins (Montomoli et al., 2001), respectively. In general, peak temperatures decrease from W to E in the Tuscan Nappe, coherently with illite crystallinity and coalification index data (Carosi et al., 2003; Cerrina Feroni et al., 1983; Reutter et al., 1978).

The Apuane and Massa units experienced a polyphase tectono-metamorphic evolution characterized by two main tectono-metamorphic stages: (1) the D1 stage attained during peak burial metamorphism (M1) and onset of exhumation, and (2) the D2 stage, interpreted as related to post–orogenic collapse/extension during retrograde metamorphism (M2) (Carmignani et al., 2001, 2004; Carmignani & Kligfield, 1990; Molli, Giorgetti, & Meccheri, 2000; Molli, Carlini, et al., 2018). The D1 stage produced a penetrative NW-SE striking and WSW-dipping S1-L1 fabric, associated with km-scale NW-SE trending isoclinal folds, well visible at map scale (Figure 1), associated with a dominantly top-to-the-NE sense of shear. The D2 stage generated open to tight recumbent F2 folds with NW-SE trending axes, associated with a sub-horizontal S2 axial-plane crenulation cleavage, marked by pressure solution seams and limited blastesis of white mica and chlorite assemblages.

The peak D1/M1 metamorphic conditions in the Apuane Unit were constrained mostly based on the X_{Mg} of chloritoid (found in Mn-rich schists) and thermo-baric estimates vary from 0.4–0.6 GPa at 350–380°C (Franceschelli et al., 1996, 1997) to ~0.8 GPa at T of 390–410°C (Jolivet et al., 1998). RSCM thermometry yielded an average temperature estimate of 397 ± 64°C (Molli, Brovarone, et al., 2018) and temperature estimates between ~330°C and 450°C were obtained through the calcite/dolomite thermometry (Di Pisa et al., 1985; Molli, Conti, Giorgetti, et al., 2000). The chloritoid- and kyanite-bearing assemblages of the Massa Unit recorded the highest peak P–T conditions during the D1/M1 stage in the Apuane metamorphic complex (Franceschelli et al., 1986). P–T estimates, based on the X_{Mg} of chloritoid, vary between $T = 420–500$°C at $P = 0.6–0.8$ GPa (Franceschelli & Memmi, 1999), $T = 400–500$°C at $P > 0.8$ GPa (Molli, Giorgetti, & Meccheri, 2000), and $T = 450–480$°C at P ~0.9 GPa (Jolivet et al., 1998). These temperature estimates are in agreement with the recent thermometric estimates obtained through RSCM thermometry, which provided an average T of 485 ± 28°C for the Massa Unit (Molli, Brovarone, et al., 2018).

The age of the D1/D2 tectono-metamorphic evolution in the Alpi Apuane is not yet fully constrained. Early $^{40}K/^{40}Ar$ and $^{40}Ar/^{39}Ar$ white mica dating yielded total gas ages of ~27 Ma for the D1 stage and plateau ages of ~13–14 Ma for the D2 stage (Kligfield et al., 1986). The ~27 Ma metamorphic ages were questioned by Patacca et al. (2013), because they overlap with the stratigraphic age of the youngest protolith involved in orogenic metamorphism in the Apuane Unit (late Oligocene-early Miocene Pseudomacigno Fm). More recently, Di Vincenzo et al. (2022) provided in-situ $^{40}Ar/^{39}Ar$ white mica ages mostly clustering in the 10–12 Ma time frame, which were interpreted to date the D2 event. In the same study, Di Vincenzo et al. (2022) suggested a minimum age of ~20 Ma for the D1/M1 stage. Zircon and apatite thermochronology indicates that (1) the Massa and Apuane Units were already tectonically coupled at 10–13 Ma (Fellin et al., 2007), before the onset of crustal thinning in the region (Molli, Carlini, et al., 2018), and (2) exhumation to shallower crustal levels was completed ~5–6 Ma. These temporal constrains indicate that the tectonic coupling of the Massa Unit with the Apuane Unit occurred during the D1/M1 stage in a contractional setting (Carmignani & Kligfield, 1990; Carosi et al., 2004; Di Vincenzo et al., 2022; Molli, Carlini, et al., 2018).

3 | METHODS

We surveyed the Massa Unit in the area between the Carrione valley to the north and the Frigido valley to the south for structural and petrographic observations with the aim to characterize the D1/M1 fabric. Twenty-three representative samples of metapelites and metapsammites, derived both from the Variscan basement and the Permian–Triassic cover, were selected for microstructural analyses (Figure 1). The list of the studied samples is available in the Supporting Information to this article (Table S1). We selected four samples of metapelite/metapsammite that displayed different parageneses (chloritoid + graphite + pyrite [field label: SP308b], chloritoid + hematite [field label: SP329], chloritoid + chlorite + hematite [field label: SP332], chloritoid + kyanite + hematite [field label: SP319]): these samples were polished for further analyses with the electron microprobe and their bulk-rock chemistry (Table 1) was obtained from the analysis of the thin section chips. Analytical details can be found in the Appendix. Additional details are provided in the supporting information, which contains a link to an online external repository hosting the mineral analyses presented in this article. Bulk rock analyses were used to calculate phase equilibrium diagrams using Perple_X. A detailed description of modelling is provided in Section 5.

4 | PETROGRAPHY AND MINERAL CHEMISTRY

Petrographic investigation through optical and electron microscopy allowed the recognition of the principal and accessory phases present in the samples and their relationships with plano-linear fabrics. In the following text and figures, white mica is used as a general term for K-(muscovite) and Na-(paragonite) white mica, because the two occupy the same microstructures and cannot be distinguished optically. Muscovite and paragonite are fine grained and intergrown, and thus differentiated only in back-scattered electron images. Mineral abbreviations are after Siivola and Schmid (2007).

4.1 | Chloritoid + graphite schist

The chloritoid + graphite schist sample (SP308b; Supporting Information) was sampled in dark grey horizons of the Palaeozoic basement (*Filladi Inferiori* Fm.; Conti et al., 2019; Figure 1), in an outcrop with evident chloritoid aggregates (Figure 2a). Bulk rock chemistry shows that the sample is a high-Al metapelite with 50.53 wt% SiO_2, 29.14 wt% Al_2O_3, 0.7 wt% MgO, and 6.01 wt% K_2O (Table 1). The measured FeO is 3.10 wt% and Fe_2O_3 is 3.31 wt% (Table 1). The rock displays the M1 chloritoid + white mica (muscovite and paragonite) + quartz + pyrite (goethitized) + graphite + rutile assemblage. Chlorite is locally present as an alteration phase after chloritoid or as irregular aggregates (Figure S1). Apatite, monazite, tourmaline, and zircon constitute common accessory phases.

Chloritoid occurs as coarse-grained radial aggregates of prismatic grains enveloped by the main S1 foliation, which is outlined by aligned white mica (predominantly muscovite, rare paragonite), quartz, graphite, and rutile grains (Figure 2b). Graphite commonly defines inclusion trails (internal foliations) within chloritoid, which are continuous with the external foliation (Figure 2c). Chloritoid also includes quartz and rutile grains (Figure 2d,e). Quartz and white mica pressure shadows commonly surround chloritoid aggregates. In places, these pressure

TABLE 1 Bulk-rock chemistry of the investigated samples and compositions used for phase equilibria modelling. See text for further details.

Sample	Cld + Gr schist	Cld + Chl + Hem schist	Cld + Hem schist	Cld + Ky + Hem schist
SiO_2	50.53	56.51	69.52	82.84
TiO_2	1.208	2.214	1.022	0.417
Al_2O_3	29.14	21.2	16.11	9.88
FeO	3.10	7.6	1.3	1.5
Fe_2O_3	3.31	4.39	4.08	2.1
MnO	0.124	0.106	0.011	0.032
MgO	0.70	0.94	0.17	0.13
CaO	0.22	0.36	0.1	0.05
Na_2O	0.76	0.29	1.31	0.2
K_2O	6.01	2.71	2.53	1.61
P_2O_5	0.19	0.19	0.07	0.01
L.O.I.	4.72	3.01	2.15	1.46
Sum	100.00	100.4	98.52	100.4

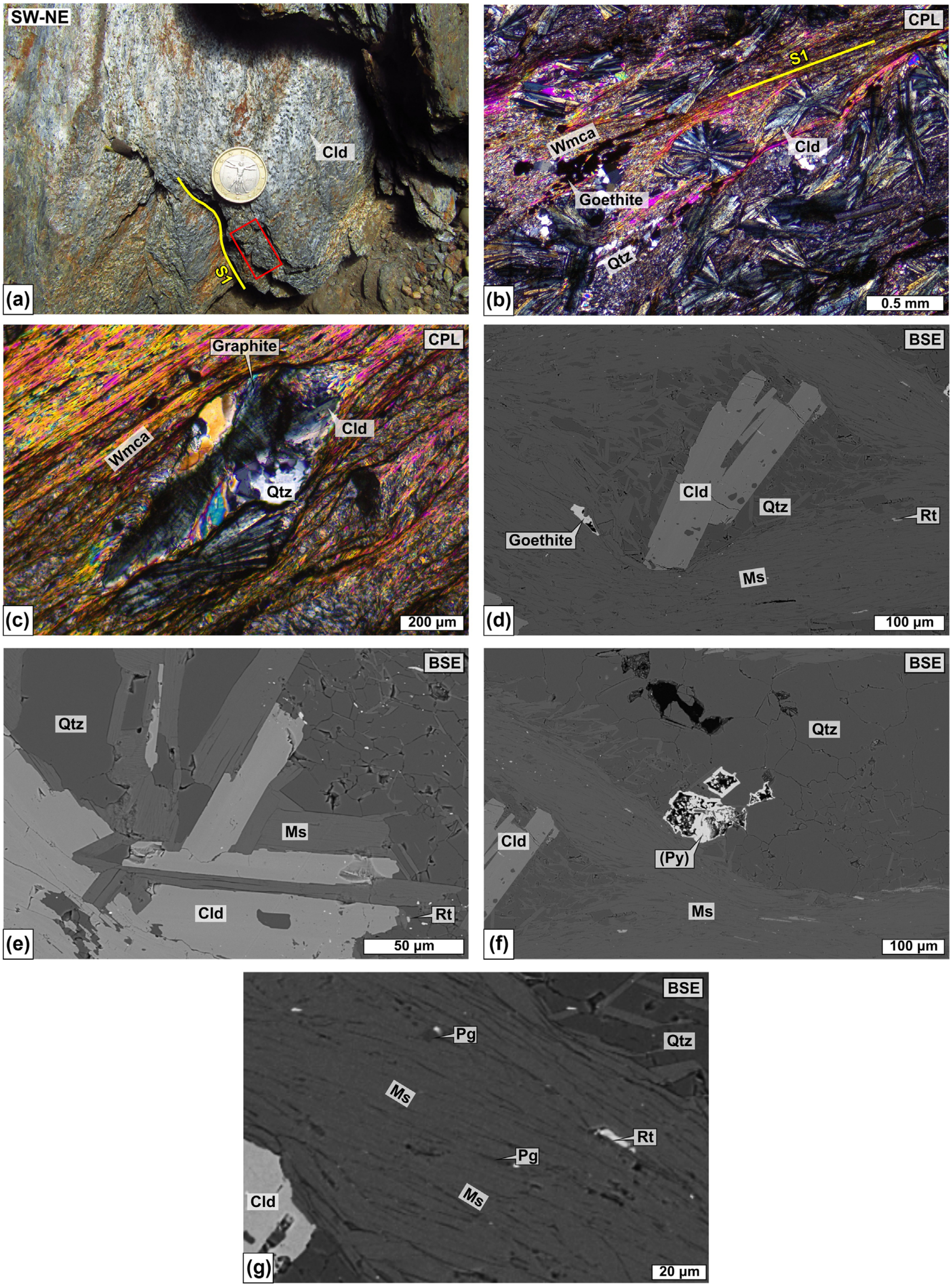

FIGURE 2 Petrography of the chloritoid + graphite schist. (a) Outcrop of Palaeozoic schists and highlighted location of the sample (red rectangle). (b) General microstructures characterized by radial aggregates of chloritoid surrounded by quartz, white mica, and goethite masses. (c) Detail of a syntectonic chloritoid aggregate (with oriented graphite trails) associated with quartz and white mica. (d) BSE image of chloritoid associated with quartz and white mica (muscovite) grains and surrounded by foliated white mica. Note the presence of rutile and goethite. (e) Detail of the equilibrium contact between chloritoid and white mica (muscovite). (f) Goethite masses with cubic (square-like) outline, interpreted as pyrite pseudomorphs. (g) BSE image with enhanced contrast highlighting the main white mica-defined foliation of the sample. Tiny, relict grains of paragonite (dark grey) are recognizable. See text for further details. Note: mineral abbreviations of minerals (after Siivola & Schmid, 2007) in this and the following figures are reported in the supporting information to this article.

shadows are truncated by graphite-rich strain caps (Figure 2c); in others they progressively fade into the surrounding foliation (Figure 2d). In both cases, these pressure shadows contain large white mica and quartz grains that preserve straight equilibrium boundaries with chloritoid (Figure 2e). Goethite occurs as square-like aggregates (Figure 2f) and as masses aligned parallel to the foliation, likely representing pseudomorphs after cubic pyrite crystals. Based on a visual estimate, these goethite aggregates cover ~2–5% of the thin section area. Paragonite is extremely rare and occurs as tiny lamellar grains (<1–5 μm thick) interspersed with muscovite (Figure 2g). These grains were too small for clean EPMA analysis and only mixed analyses were obtained (see below).

Chloritoid (Table 2) is characterized by a X_{Mg} (=Mg apfu/[Mg apfu + Fe_{TOT} apfu]; apfu = atoms per formula unit) of 0.12–0.15. In general, we observe higher X_{Mg} values closer to the rims (0.14–0.15), whereas cores are typically enriched in Fe (X_{Mg} = 0.12–0.13). However, core and rim compositions overlap in many grains. The Mn content in chloritoid is between 0.02–0.03 apfu with X_{Mn} (= Mn apfu/[Mg apfu + Mn apfu + Fe apfu]), usually around or less than 0.01, from core to rim (Figure 6a). The recalculated chloritoid composition shows Fe^{3+} contents close to 0 (Table 2 and online repository).

White mica has a composition close to the muscovite end-member, with X_{Na} (= Na apfu/[K apfu + Na apfu + Ca apfu]) < 0.20 (Figures 6b and 7a) and a Si content between 3.03 and 3.09 apfu, lying on the muscovite–celadonite (phengite) series (Figure 6c). Outliers with X_{Na} = 0.23 and 0.47 are interpreted as mixed muscovite–paragonite analyses, since they lie in the 0.20–0.70 range, which corresponds to the muscovite–paragonite solvus, according to Guidotti et al. (1994). The X_{Mg} of white mica ranges from 0.46 to 0.68 (Figures 7d and 8a). Ti, Mn, and Ca are usually present as trace elements (<0.01 apfu). A correlation exists between X_{Na}, X_{Mg}, and the Si apfu content: white micas with high X_{Na} (= 0.14–0.19) show lower Si apfu (3.02–3.06) and X_{Mg} (0.46–0.54) compared to those with low X_{Na} (0.10–0.14), which, are characterized by high Si apfu (3.06–3.10) and X_{Mg} (0.54–0.68) instead (Figures 7a,d and 8a). Notably, we did not detect any discernible difference in composition between the white mica grains aligned on the foliation and those occurring in the pressure shadows around chloritoid. Rutile composition is almost pure TiO_2 with minor Si and Fe impurities (<0.01 apfu) (Table 3).

4.2 | Chloritoid + chlorite + hematite schist

This sample (SP332; see supporting information) is a light grey metapsammite from the Permian–Triassic succession (Figures 1 and 3a). It is a high Al-metapelite (SiO_2 = 56.51 wt%; Al_2O_3 = 21.2 wt%) with relatively high FeO content (7.6 wt%), 4.39 wt% Fe_2O_3, and low MgO (0.94 wt%), and K_2O (2.71 wt%) (Table 1). It contains the chloritoid + chlorite + white mica (muscovite only) + quartz + hematite + rutile M1 assemblage (Figure 3b); accessory phases are epidote, allanite, tourmaline, apatite, monazite, and zircon.

Chloritoid grains show coarse grain size (mm scale), while phyllosilicates (white mica and chlorite) are fine grained, generally around 100 μm (Figure 3b,c). Chloritoid and chlorite grains are intimately associated in aggregates, together with white mica, hematite, and quartz, and commonly display straight, equilibrium boundaries (Figure 3c,d). Within these aggregates, white mica consists of coarse-grained, euhedral grains associated with chlorite and chloritoid (Figure 3d). The enveloping matrix is composed of white mica, quartz, and hematite with minor chlorite, all aligned along the main S1 foliation (Figure 3b). Chloritoid is rich in hematite inclusions, often organized in sectors or concentrated in specific twins (ottrelite-like patterns; Figure 3b,c). Other common inclusions consist of quartz, rutile, and accessory minerals. Epidote is present as an accessory phase that typically contains an allanite core and can be found intergrown with chloritoid (Figure 3e). Rutile is commonly found as epitaxial needle-like inclusions within hematite (Figure 3e).

Chloritoid grains are zoned and show Fe-rich cores and Mg-rich rims (X_{Mg} = 0.10–0.14; Figure 6a). Mn is chiefly fractionated in the cores, where it reaches X_{Mn} contents of 0.02–0.03 (Table 2). The recalculated Fe^{3+} ranges between 0.00 and 0.10 and no correlation exists between the Fe^{3+} content and the X_{Mg} (Table 2 and online repository).

White mica shows phengitic composition, close to the muscovite end-member, with X_{Na} = 0.10–0.20, Si = 3.00–3.10 apfu, and X_{Mg} = 0.17–0.33 (Figures 6b,d, 7b,e, and 8b). On the (Fe + Mg) apfu–Si apfu diagram, white mica analyses plot slightly below the muscovite–celadonite series, towards the trioctahedral mica end-member (Figure 6d). The Si apfu and X_{Mg} content both correlate with the X_{Na}. In particular, white micas with high X_{Na} (0.14–0.18) are characterized by low Si apfu (3.00–3.05) and X_{Mg} (0.15–0.25), whereas those with low X_{Na} (<0.14) generally display higher Si apfu (>3.05) and X_{Mg} (up to 0.33) values (Figures 7b,d and 8b). We did not detect paragonite in this sample. Chlorite shows nearly constant composition, with octahedral Al comprised between 1.50 and 1.70 apfu, and X_{Mg} = 0.36–0.42 (Figure 6g): the Mn content is generally low (<0.01–0.02 apfu) and Ti is present in trace amounts (<0.01 apfu).

Hematite is titaniferous and may contain up to 7–8 wt% TiO_2 (Table 3). Rutile has nearly pure composition

TABLE 2 Representative analyses of silicate minerals from the investigated samples, recalculated on 11 (white micas), 14 (chlorite), 12 (chloritoid), and 5 (kyanite) oxygen basis. Details about the recalculation of FeO/Fe_2O_3 are provided in the 'Methods' section.

Sample	Cld + Gr schist			Cld + Hem schist			Cld + Hem schist			Cld + Ky + Hem schist		
Phase	Ms	Ms	Ms	Ms	Ms	Ms	Ms	Pg	Ms	Ms	Pg	Prl
Analysis n	wm3	wm18	wm87	S2-11	S2-40	S189	S026	S037	S058	wm20	wm20	wm43
SiO_2	46.61	46.08	46.40	45.33	44.79	46.28	47.07	47.63	46.82	46.07	46.90	66.01
TiO_2	0.11	0.13	0.11	0.17	0.16	0.19	0.05	0.04	0.06	0.06	0.02	0.04
Al_2O_3	36.37	37.15	35.86	34.69	35.46	33.88	36.92	40.15	37.01	35.79	40.19	29.27
Cr_2O_3	-	-	-	0.00	0.05	0.02	0.03	0.01	0.05	-	-	-
FeOtot	1.01	1.22	0.95	3.10	2.95	3.55	1.60	0.74	1.88	1.91	0.85	0.45
MnO	0.07	0.13	0.00	0.00	0.05	0.00	0.00	0.05	0.01	0.07	0.06	0.00
MgO	0.58	0.76	0.87	0.37	0.36	0.87	0.30	0.10	0.30	0.34	0.05	0.03
CaO	0.00	0.00	0.01	0.00	0.00	0.00	0.02	0.12	0.00	0.07	0.14	0.04
BaO	0.17	0.09	0.16	0.21	0.19	0.14	0.06	0.02	0.09	0.05	0.04	0.00
Na_2O	1.16	0.79	0.90	0.96	0.89	0.81	1.68	5.25	1.53	0.95	5.94	0.07
K_2O	8.74	9.22	8.92	9.53	9.80	9.36	8.19	2.48	8.62	8.80	1.88	0.17
Total	**94.82**	**95.56**	**94.18**	**94.35**	**94.70**	**95.10**	**95.92**	**96.59**	**96.37**	**94.12**	**96.07**	**96.08**
Si	3.08	3.04	3.09	3.07	3.03	3.11	3.08	3.01	3.06	3.08	2.98	3.94
Al^{IV}	0.92	0.96	0.91	0.93	0.97	0.89	0.92	0.99	0.94	0.92	1.02	0.06
Al^{VI}	1.92	1.92	1.91	1.84	1.85	1.79	1.92	2.00	1.91	1.91	2.00	1.99
Cr	-	-	-	0.00	0.00	0.00	0.00	0.00	0.00	-	-	-
Ti	0.01	0.01	0.01	0.01	0.01	0.01	0.00	0.00	0.00	0.00	0.00	0.00
Fe^{2+}	0.06	0.07	0.05	0.18	0.17	0.20	0.09	0.04	0.10	0.11	0.05	0.02
Mn	0.00	0.01	0.00	0.00	0.00	0.00	0.00	0.00	0.00	0.00	0.00	0.00
Mg	0.06	0.07	0.09	0.04	0.04	0.09	0.03	0.01	0.03	0.03	0.00	0.00
Ca	0.00	0.00	0.00	0.00	0.00	0.00	0.00	0.01	0.00	0.00	0.01	0.00
Ba	0.00	0.00	0.00	0.01	0.00	0.00	0.00	0.00	0.00	0.00	0.00	0.00
Na	0.15	0.10	0.12	0.13	0.12	0.10	0.21	0.64	0.19	0.12	0.73	0.01
K	0.74	0.77	0.76	0.82	0.84	0.80	0.68	0.20	0.72	0.75	0.15	0.01

Sample	Cld + Gr schist			Cld + Chl + Hem schist			Cld + Hem schist			Cld + Ky + Hem schist		
Phase	Cld	Cld	Cld	Cld	Cld	Chl	Cld	Cld	Cld	Cld	Cld	Ky
Location	core	core	rim	core	rim	-	core	mid	rim	core	rim	-
Analysis n	k5	k8	k44	S128	S148	S2-17	S98	S6	S17	S2-71	S2-76	k3
SiO_2	23.95	24.20	24.07	23.50	23.87	23.27	24.18	24.33	23.91	23.61	24.32	36.89
TiO_2	0.41	0.03	0.06	0.06	0.02	0.08	0.00	0.00	0.20	0.02	0.02	0.02
Al_2O_3	39.65	40.81	40.33	39.70	39.92	22.31	40.88	40.48	40.20	38.78	41.04	63.19
Cr_2O_3	0.02	0.00	0.02	0.01	0.04	0.09	0.06	0.00	0.02	0.06	0.00	0.00
FeOtot	24.36	23.65	23.47	25.29	24.62	29.34	22.34	21.14	24.70	21.94	17.65	0.47
MnO	0.33	0.32	0.30	0.77	0.32	0.14	0.34	0.44	0.09	1.00	0.61	0.00
MgO	1.85	2.16	2.28	1.56	2.19	10.40	3.24	4.47	2.04	3.21	6.58	0.02
CaO	0.00	0.01	0.01	0.00	0.01	0.02	0.02	0.02	0.01	0.01	0.00	0.01
BaO	-	0.00	0.00	0.00	0.00	0.04	0.01	0.00	0.02	0.02	0.02	-
Na_2O	0.01	0.02	0.00	0.00	0.03	0.06	0.03	0.03	0.00	0.00	0.00	0.02
K_2O	0.02	0.02	0.00	0.00	0.01	0.12	0.00	0.00	0.00	0.00	0.01	0.04
Total	**90.61**	**91.22**	**90.55**	**90.97**	**91.09**	**85.86**	**91.08**	**90.97**	**91.18**	**88.69**	**90.36**	**100.71**

TABLE 2 (Continued)

Sample	Cld + Gr schist			Cld + Chl + Hem schist			Cld + Hem schist			Cld + Ky + Hem schist		
Phase	Cld	Cld	Cld	Cld	Cld	Chl	Cld	Cld	Cld	Cld	Cld	Ky
Location	core	core	rim	core	rim	-	core	mid	rim	core	rim	-
Analysis n	k5	k8	k44	S128	S148	S2-17	S98	S6	S17	S2-71	S2-76	k3
Si	2.02	2.02	2.02	1.99	2.01	2.57	2.01	2.01	2.01	2.02	1.99	0.99
Al	3.95	4.01	3.99	3.96	3.95	2.91	4.00	3.94	3.98	3.92	3.96	2.00
Cr	0.00	0.00	0.00	0.00	0.00	0.01	0.00	0.00	0.00	0.00	0.00	0.00
Ti	0.03	0.00	0.00	0.00	0.00	0.01	0.00	0.00	0.01	0.00	0.00	0.00
Fe^{2+}	1.72	1.65	1.65	1.74	1.70	2.71	1.55	1.42	1.73	1.54	1.14	-
Fe^{3+}	0.00	0.00	0.00	0.05	0.03	-	0.00	0.04	0.00	0.03	0.07	0.01
Mn	0.02	0.02	0.02	0.06	0.02	0.01	0.02	0.03	0.01	0.07	0.04	0.00
Mg	0.23	0.27	0.29	0.20	0.27	1.72	0.40	0.55	0.25	0.41	0.80	0.00
Ca	0.00	0.00	0.00	0.00	0.00	0.00	0.00	0.00	0.00	0.00	0.00	0.00
Ba	-	-	-	0.00	0.00	0.00	0.00	0.00	0.00	0.00	0.00	-
Na	0.00	0.00	0.00	0.00	0.01	0.01	0.00	0.00	0.00	0.00	0.00	0.00
K	0.00	0.00	0.00	0.00	0.00	0.02	0.00	0.00	0.00	0.00	0.00	0.00

but may contain impurities of FeO, SiO_2, and Al_2O_3. Epidote shows a high pistacite content ($Fe^{3+} = 0.70$–0.76 apfu) (see online repository).

4.3 | Chloritoid + hematite schist

The chloritoid + hematite schist sample (SP329; see supporting information) was collected from quartz-rich (white) layers in a succession of light grey to dark violet metapelites and metapsammites from the Permian–Triassic cover (Figures 1 and 4a). Its composition is that of a high-Al metapsammite with 69.52 wt% SiO_2 and 16.11 wt% Al_2O_3. The content of MgO is 0.17 wt%, K_2O is 2.53 wt%, and Na_2O is 1.31 wt% (Table 1). Interestingly, the sample has only 1.30 wt% FeO and very high Fe_2O_3 ~4.08 wt% (Table 1).

The M1 assemblage consists of chloritoid + white mica (muscovite and paragonite) + quartz + hematite + rutile, with accessory tourmaline, apatite, and zircon (Figure 4b–d). Chloritoid occurs as coarse-grained, euhedral, and prismatic aggregates, surrounded by alternating fine-grained white mica-rich and medium- to coarse-grained quartz-rich layers, aligned along the main S1 foliation (Figure 4b). Quartz is also commonly present in pressure shadows around chloritoid grains (Figure 4c). Hematite lamellae are common in the mica-rich layers and occur oriented parallel to the S1, whereas rutile is present as aggregates (Figure 4c). Chloritoid frequently contains inclusions of quartz, hematite, rutile, and other accessory minerals (Figure 4d). The mica-defined foliation consists of subparallel grains of muscovite and paragonite, which are finely intergrown (Figure 4e,f). In general, muscovite consists of larger grains occurring aligned on the foliation (Figure 4e) and within quartz-rich domains (Figure 4f), whereas paragonite grains are smaller and frequently occur as blebs/lamellae within muscovite (Figure 4e,f; Na-map of Figure 4g). This textural association hampered the analysis of individual paragonite grains (see below).

The composition of chloritoid (Table 2) ranges from $X_{Mg} = 0.13$ to 0.27, with $X_{Mn} < 0.01$–0.02 (Figure 6a). Compositional zoning is complex, with X_{Mg} first increasing from 0.16–0.20 in the core to values of 0.23–0.27 halfway between the core and the rim (mantle in Figure 6h) and then decreasing to values of 0.13–0.14 in the rims (Figures 4g,h and 6a,h). Most of the chloritoid analyses show recalculated Fe^{3+} contents close to 0 and a limited scattering up to 0.07 Fe^{3+} apfu, uncorrelated with the X_{Mg} value (Table 2 and online repository).

Due to the fine-grained intergrowth of muscovite and paragonite, we could not resolve the composition of paragonite, and most of the analyses show X_{Na} comprised between 0.10 and 0.80, occurring within the solvus range determined by Guidotti et al. (1994) and thus representing mixed analyses (Figures 6b and 7g,h). K-white mica analyses are characterized by Si between 3.00 and 3.10 apfu and lie close to the muscovite end-member on the phengite series (Figures 6e and 7g). Their X_{Mg} clusters between 0.10 and 0.30 (Figure 7h) and correlates with the

TABLE 3 Representative analyses of oxides and hydroxides, recalculated on 2 (rutile), 3 (hematite), and 1.5 (goethite) oxygen basis. Check the 'Methods' section for further details.

Sample	**Cld + Gr schist**		**Cld + Chl + Hem schist**		**Cld + Hem schist**		**Cld + Ky + Hem schist**	
Phase	**Rt**	**Gt**	**Rt**	**Hem**	**Rt**	**Hem**	**Rt**	**Hem**
Analysis n	ox1	ox6	O52	O60	O1	O17	ox11	ox1
SiO_2	0.13	2.24		0.13	0.11	0.57	0.31	0.09
TiO_2	97.61	0.06	97.45	8.25	98.70	2.88	96.71	2.14
Al_2O_3	0.08	1.80	0.06	0.10	0.09	0.36	0.07	0.10
V_2O_3	-	-	-	-	-	-	0.47	0.09
Cr_2O_3	-	-	0.06	0.05	0.08	0.08	0.12	0.01
FeOtot	0.87	-	1.43	-	0.82	-	0.96	-
Fe_2O_3tot	-	75.83		89.86	-	94.54	-	96.73
MnO	0.01	1.00	0.00	0.01	0.03	0.01	0.01	0.01
NiO	-	-	-	-	-	-	0.02	0.01
MgO	0.00	0.35	0.01	0.00	0.00	0.00	0.00	0.01
CaO	0.05	0.77	0.00	0.00	0.03	0.05	0.01	0.00
ZnO	-	-	-	-	-	-	0.00	0.00
CoO	-	-	-	-	-	-	0.00	0.08
CuO	-	-	-	-	-	-	0.01	0.02
Total	**98.76**	**82.04**	**99.20**	**98.40**	**99.94**	**98.46**	**98.70**	**99.28**
Si	0.00	0.04	0.00	0.00	0.00	0.02	0.00	0.00
Al	0.00	0.03	0.00	0.00	0.00	0.01	0.00	0.00
V	-	-	-	-	-	-	0.01	0.00
Cr	-	-	0.00	0.00	0.00	0.00	0.00	0.00
Ti	0.99	0.00	0.99	0.16	0.99	0.06	0.98	0.04
Fe^{2+}	0.01	0.00	0.02	-	0.01	-	0.01	-
Fe^{3+}	-	0.90	-	1.77	-	1.89	-	1.93
Mn	0.00	0.01	0.00	0.00	0.00	0.00	0.00	0.00
Mg	0.00	0.01	0.00	0.00	0.00	0.00	0.00	0.00
Ca	0.00	0.01	0.00	0.00	0.00	0.00	0.00	0.00
Zn	-	-	-	-	-	-	0.00	0.00
Co	-	-	-	-	-	-	0.00	0.00
Cu	-	-	-	-	-	-	0.00	0.00

Si apfu content, with high X_{Mg} compositions corresponding to higher Si apfu values (Figure 8c). Paragonitic compositions tend to display lower X_{Mg} and Si apfu (Figure 7g,h). Hematite is titaniferous (Figure 4j) and contains up to 2–3 wt% TiO_2. Rutile may contain up to 2 wt% FeO and SiO_2 and minor Al_2O_3 (Table 3).

4.4 | Chloritoid + kyanite + hematite schist

This sample (SP319; see supporting information) is from silver grey schists with millimetric prismatic kyanite grains (well visible at outcrop scale) interlayered within Triassic metabreccias (Figure 5a). The composition of this sample is characterized by high SiO_2 (82.84 wt%) and Al_2O_3 (9.88 wt%) contents and minor K_2O (1.61 wt%). MgO is present in very small amounts (0.13 wt%) (Table 1). This sample shows an elevated Fe_2O_3 content of 2.1 wt% and only 1.5 wt% FeO (Table 1).

At the microscale, the M1 assemblage consists of kyanite + chloritoid + white mica (muscovite + paragonite) + pyrophyllite + quartz + hematite + rutile (Figure 5b–f); accessory minerals are tourmaline, zircon, and apatite. Kyanite is coarse-grained and generally euhedral, displaying an average grain size of ~200–300 μm.

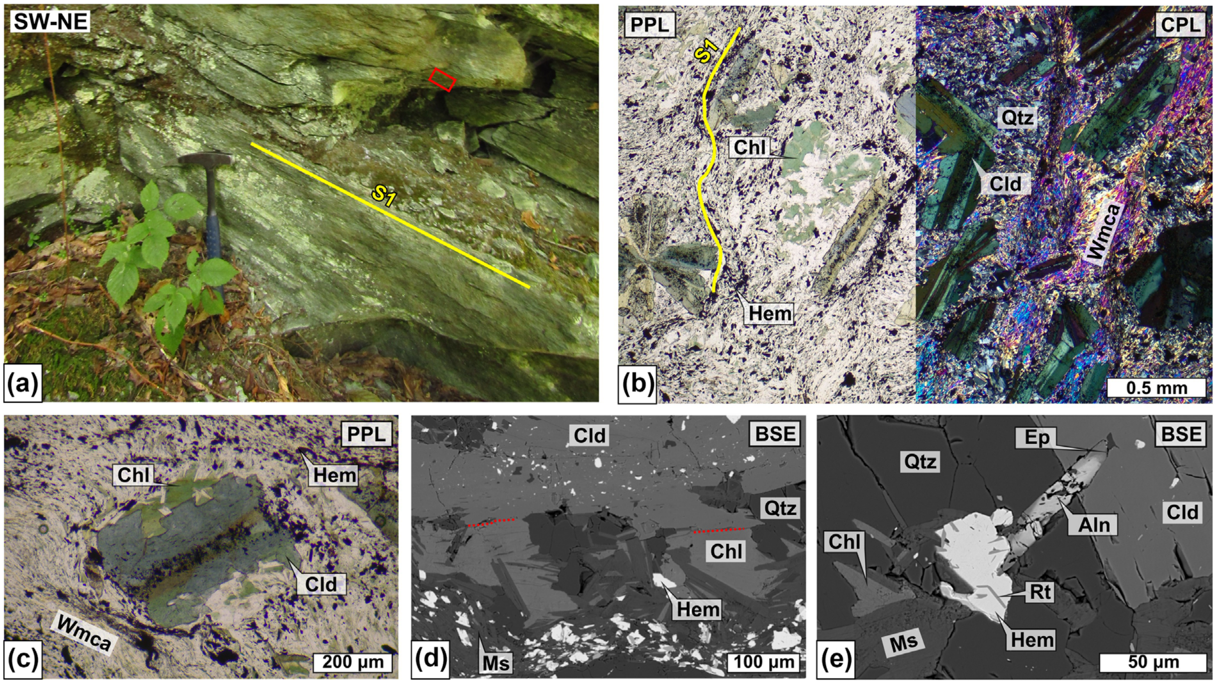

FIGURE 3 Petrography of the chloritoid + chlorite + hematite schist. (a) Outcrop of Permian–Triassic schist and location of the investigated sample. (b) General microstructure, characterized by aggregates of chloritoid + chlorite grains associated with quartz, white mica (muscovite), and hematite. (c) Detail of a chloritoid + chlorite aggregate showing equilibrium boundaries between chlorite and chloritoid. Note the presence of hematite inclusions in the chloritoid core. (d) BSE image highlighting the association of chloritoid, chlorite, white mica (muscovite), quartz, and hematite. (e) Detail of an epidote grain with an allanite core, partly surrounded by chloritoid, and rutile–hematite aggregates. See text for further details.

Chloritoid grains are smaller, ranging from 20 to 100 μm (Figure 5b,c). Kyanite and chloritoid grains are surrounded by alternating fine- to medium-grained quartz-rich and mica-rich domains, defining the S1 foliation and containing lamellar hematite (Figure 5b,c). Hematite and rutile occur dispersed in the matrix and as inclusions within chloritoid and kyanite (Figure 5d,e), together with quartz and white mica (e.g., K-map in Figure 5k). White mica almost exclusively consists of K-white mica (muscovite). Paragonite is very rare and present mostly as rounded and irregular blebs of a few micrometres surrounded by K-white mica (Figure 5f). Pyrophyllite is also locally found as masses and blebs interweaved with muscovite (Figure 5g).

Chloritoid grains are strongly zoned and show Fe- and Mn-rich cores surrounded by Mg-rich rims (Figure 5h–k). A very thin (few μm thick) Fe-rich rim is also locally present (Figure 5j). X_{Mg} values range from 0.17–0.18 (core) to ~0.40 (rim), while X_{Mn} varies from 0.02–0.04 (core) to 0.00–0.01 (rim) (Figure 6a). Recalculated Fe^{3+} contents range from 0.00 up to 0.10 (Table 2 and online repository).

The analysed K-white micas show X_{Na} between 0.10 and 0.20. We also obtained a single paragonite analysis with $X_{Na} = 0.83$ (Figure 6b) from a paragonite relic. White mica shows Si largely comprised between 3.02 and 3.10 apfu and phengitic composition with ~0.12–0.16 Fe + Mg apfu (Figure 6f). In the diagram of Figure 6f, it is also possible to observe the analysed composition of pyrophyllite, characterized by Si apfu > 3.90 and Fe + Mg apfu < 0.04. The X_{Mg} of white mica is comprised between 0.20 and 0.30 (Figure 7f). Differently from the other samples, we do not observe a clear correlation between the X_{Na}, X_{Mg}, and Si apfu content of white mica (Figures 7c,f and 8d). Kyanite occurs as a nearly pure phase, containing ~0.01 apfu Fe^{3+} (Table 2). Hematite is titaniferous (TiO_2 = 1.5–2.5 wt%). Rutile contains up to 2 wt% FeO (Table 3).

5 | PHASE EQUILIBRIA MODELLING

Bulk rock analyses were used to calculate phase equilibrium diagrams using the software Perple_X version 6.9.1, source updated 10 November 2021 (Connolly, 2005, 2009), and the HP62 version of the internally consistent data set (Holland & Powell, 2011).

We used the following solution models (as named in the Perple_X solution model file): Bi(W)—biotite,

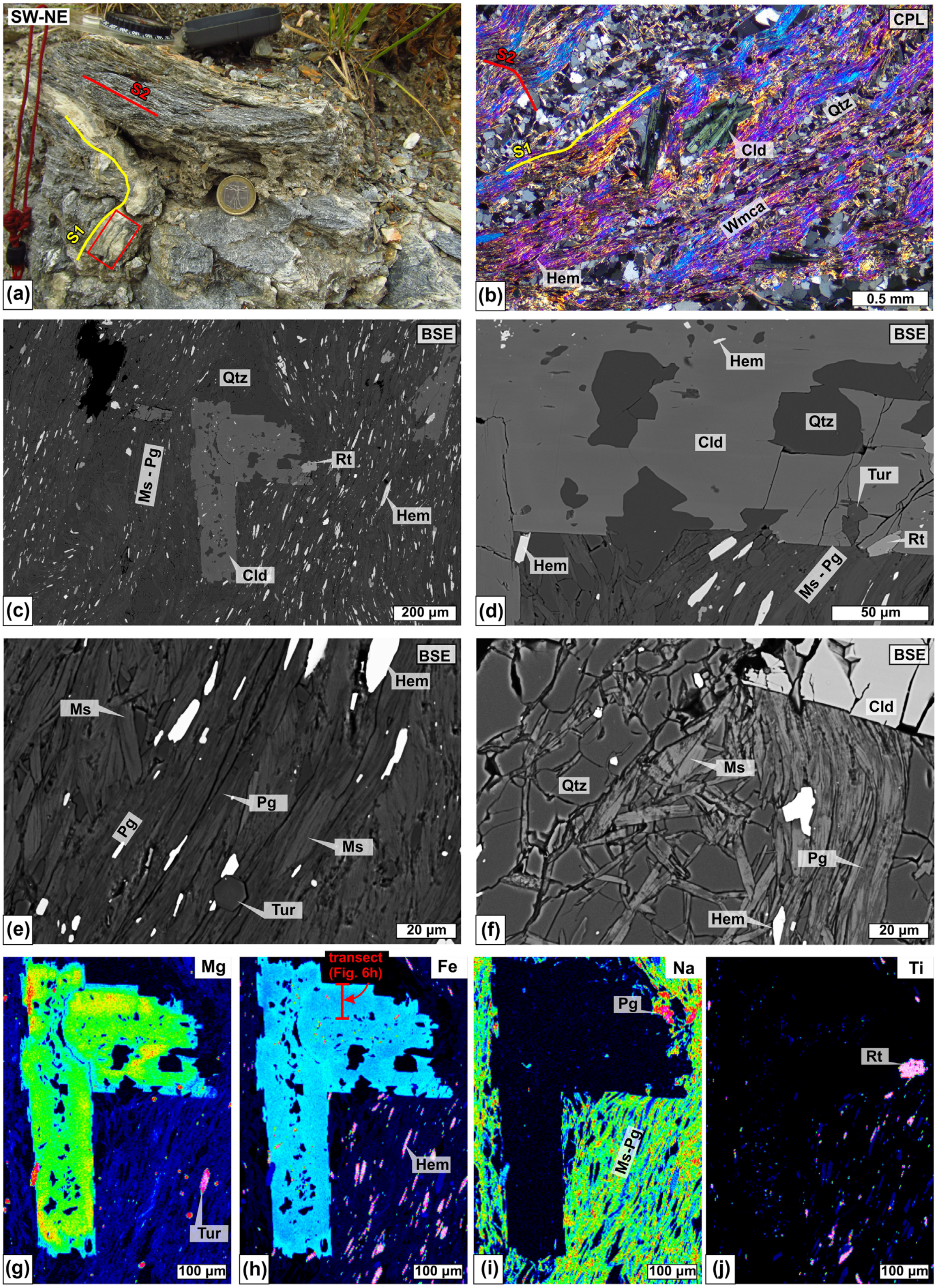

FIGURE 4 Petrography of the chloritoid + hematite schist. (a) Sampling site located in the hinge zone of folded Permian–Triassic schists. (b) General microstructure, marked by chloritoid grains, surrounded by lepidoblastic white mica (muscovite + paragonite) layers and granoblastic quartz-rich layers. (c) BSE image highlighting a chloritoid + quartz aggregate surrounded by foliated white mica (muscovite + paragonite) + hematite and associated with rutile grains. (d) Detail of (c) showing hematite, quartz, rutile, and tourmaline inclusions in chloritoid. (e-f) Enhanced-contrast BSE images showing interweaved paragonite (dark-coloured) and muscovite (light-coloured) grains in mica-rich domains. Note that paragonite always occurs as tiny blebs/lamellae associated with muscovite. (g–j) X-ray maps of (g) Mg, (h) Fe, (i) Na, and (j) Ti for the chloritoid aggregate shown in (c). See text for further details.

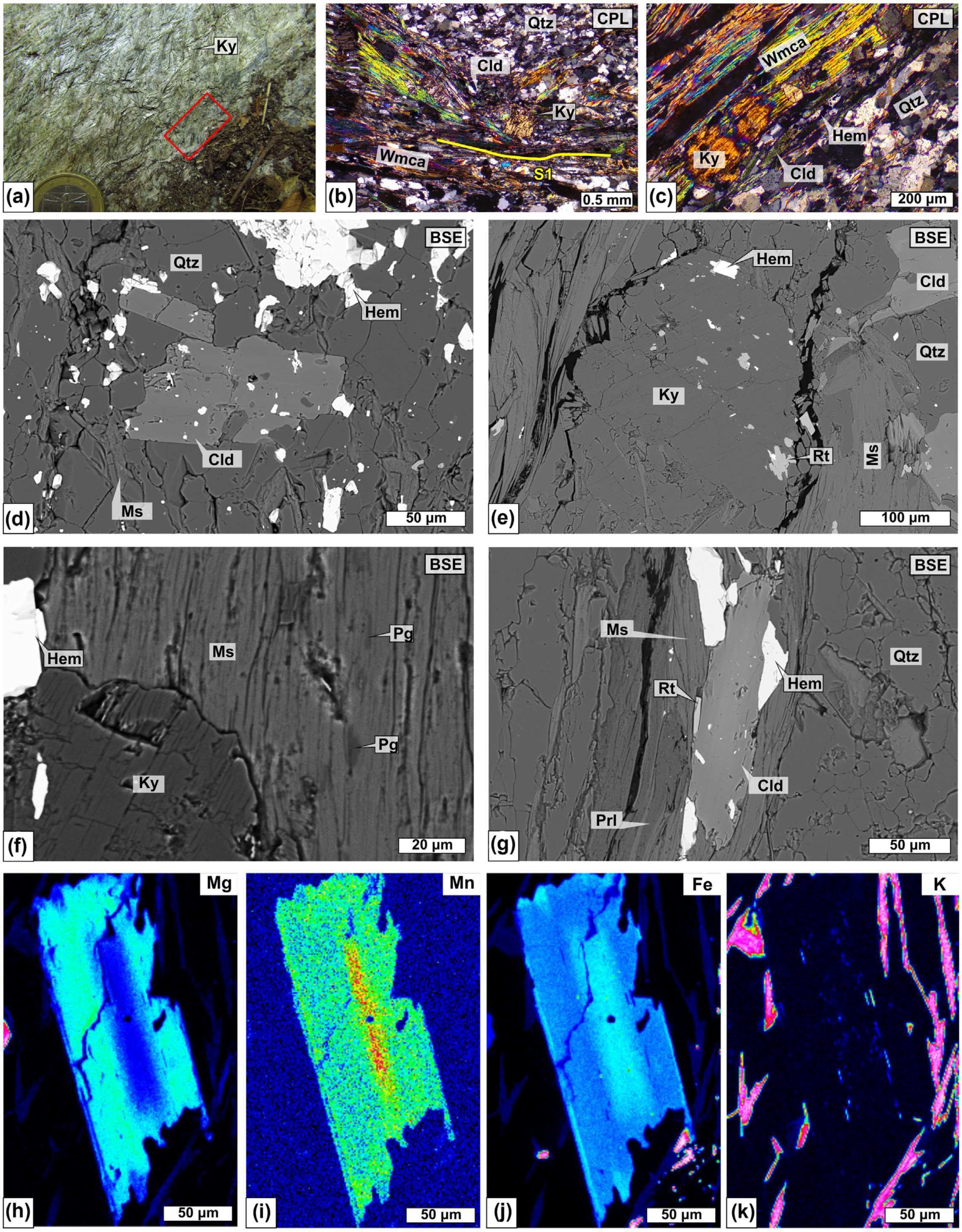

FIGURE 5 Petrography of the chloritoid + kyanite + hematite schist. (a) Sampling site (outcrop of Permian–Triassic metabreccia), with visible kyanite grains. (b,c) Microphotographs showing kyanite and chloritoid grains in association with white mica, quartz, and hematite. (d–g) BSE images showing (d) chloritoid grains with hematite inclusions, surrounded by quartz and hematite, (e) a kyanite grain with rutile and hematite inclusions, associated with quartz, chloritoid, and white mica, (f) relict paragonite grains surrounded by muscovite close to a large kyanite grain, and (g) a chloritoid grain in contact with hematite and rutile, associated with white mica and blebs of pyrophyllite. (h–k) X-ray maps of (h) Mg, (i) Mn, (j) Fe, and (k) K highlighting the zoning of a chloritoid grain.

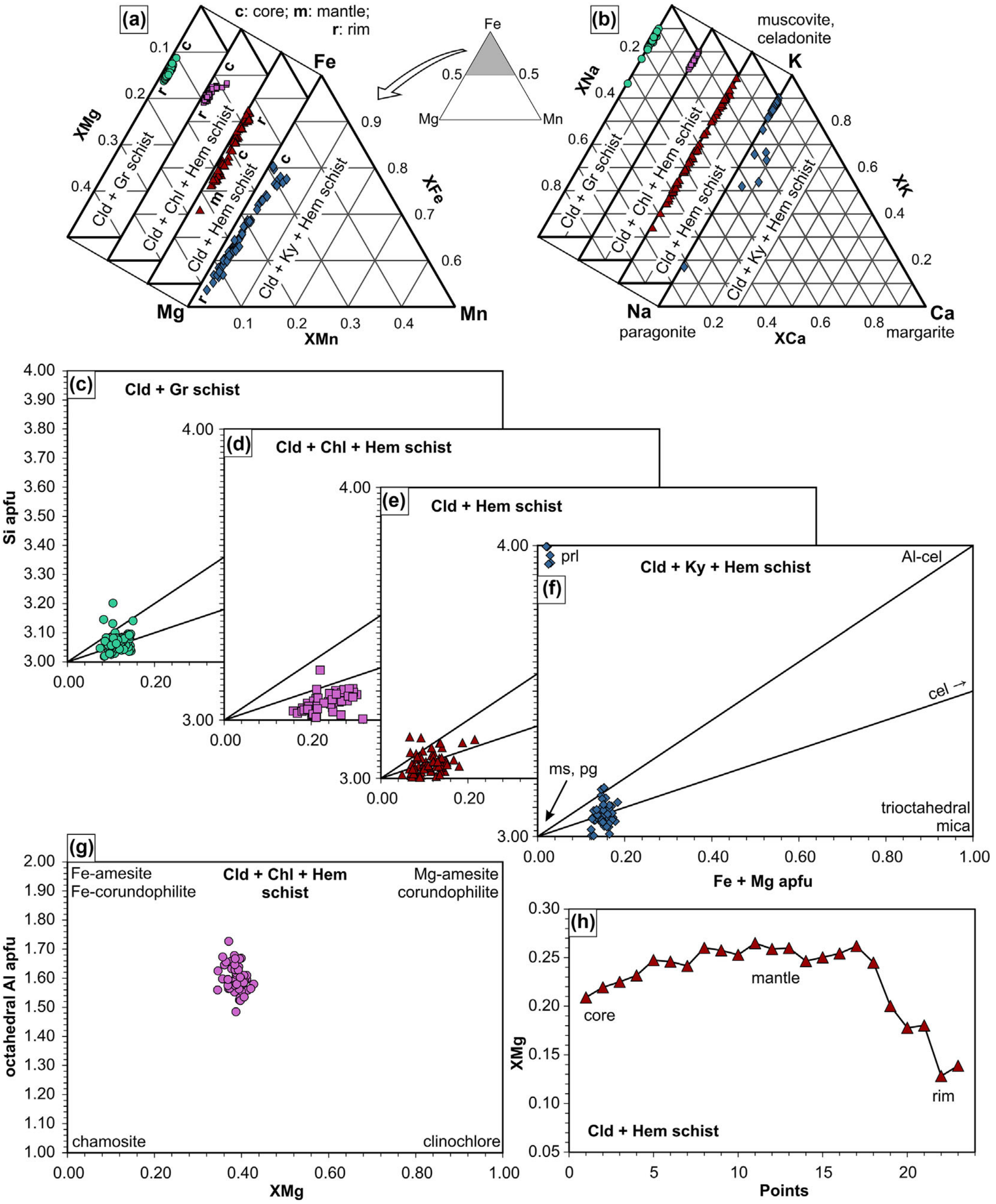

FIGURE 6 Chloritoid and white mica chemistry in the investigated samples. (a-b) Ternary diagrams showing (a) the Fe–Mg–Mn composition of chloritoid and (b) the K–Na–Ca composition of white mica. In (a), c = core, r = rim, m = mantle (i.e., halfway between core and rim). (c-d-e-f) Fe + Mg apfu–Si apfu plots for white mica in the (c) chloritoid + graphite, (d) chloritoid + chlorite + hematite, (e) chloritoid + hematite, and (f) chloritoid + kyanite + hematite schist samples. (g) X_{Mg}–octahedral Al apfu diagram showing the composition of chlorite in the chloritoid + chlorite + hematite sample. (h) Core to rim point analyses transect for the chloritoid grain shown in Figure 4g. Step: 1 point every 3 μm.

Mica(W)—K, Na white mica, Chl(W)—chlorite, Ctd(W)—chloritoid, St(W)—staurolite, Crd(W)—cordierite, Gt(W)—garnet, Opx(W)—orthopyroxene, Ep (HP11)—epidote, Ilm (DS6)—ilmenite/hematite, Sp (WPC)—spinel (including magnetite), T—talc, feldspar—ternary feldspar, and Carp(M)—carpholite (Fuhrman & Lindsley, 1988; Holland & Powell, 2011; Massonne & Willner, 2008; White et al., 2000, 2002, 2014). For all calculations we assumed H_2O in excess and CO_2 is not considered in the system.

The implemented Mica(W) model does not include Mn-bearing end-members: this caused an issue with the chloritoid + graphite and chloritoid + chlorite + hematite samples, where garnet appeared at unusual

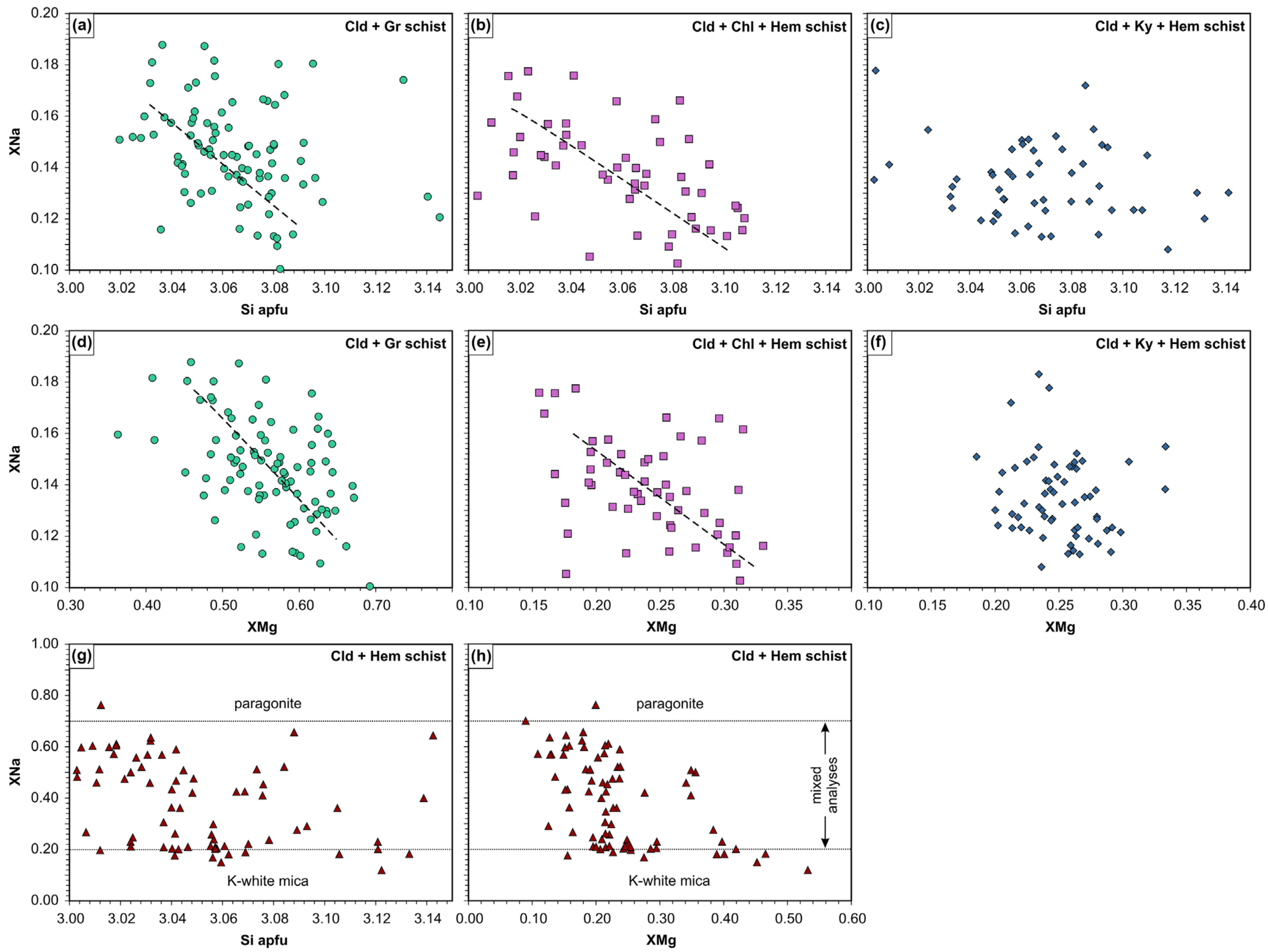

FIGURE 7 White mica chemistry. (a-b-c-g) Si apfu–X_{Na} plots and (d-e-f-h) X_{Mg}–X_{Na} plots for K-Na-white mica in the (a-d) chloritoid + graphite, (b-e) chloritoid + chlorite + hematite, (c-f) chloritoid + kyanite + hematite, and (g-h) chloritoid + hematite schist samples. Dashed lines highlight the best linear fit for the data points.

low T ($T < 350°C$), incorporating Mn as a spessartine component. Alternatively, the predicted 'over-stability' of garnet may be due to uncertainties in the activity-composition relationships for Mn end-members; however, low-T spessartine garnet are observed in many chlorite-grade rocks (see discussion in White et al., 2014). More likely, nucleation may be delayed to higher T conditions by reaction overstepping (e.g., Spear & Pattison, 2017). Consequently, to reproduce the observed garnet-free assemblages, we calculate pseudosections for chloritoid + graphite and chloritoid + chlorite + hematite schists without Mn, using the K_2O–FeO–MgO–Al_2O_3–SiO_2–H_2O–TiO_2–O (NKFMASHTO) chemical system, using the chemical compositions and contents of Fe_2O_3 reported in Table 1.

The calculated pseudosection all reproduce well the mineral assemblages, modes, and chemistry of the analysed samples, except for the chloritoid + graphite schist, whose bulk rock composition appears to have been altered by oxidation (more details in Section 5.1). Therefore, it was necessary to calculate P–T–X pseudosections only for this sample to correctly estimate the appropriate content of Fe_2O_3 for phase equilibrium modelling.

5.1 | Chloritoid + graphite schist

The bulk-rock analyses show an elevated Fe_2O_3 content (3.32 wt% of Fe_2O_3 and 3.1 wt% FeO). This is in contrast with the presence of graphite and lack of hematite in this sample. The occurrence of goethitized pyrite (Figure 2f), indicative of oxidative weathering, suggests the measured Fe_2O_3 content is higher than the actual reactive bulk composition during metamorphism. Consequently, the bulk rock Fe_2O_3 content should be modified to reflect the composition prior to oxidative weathering.

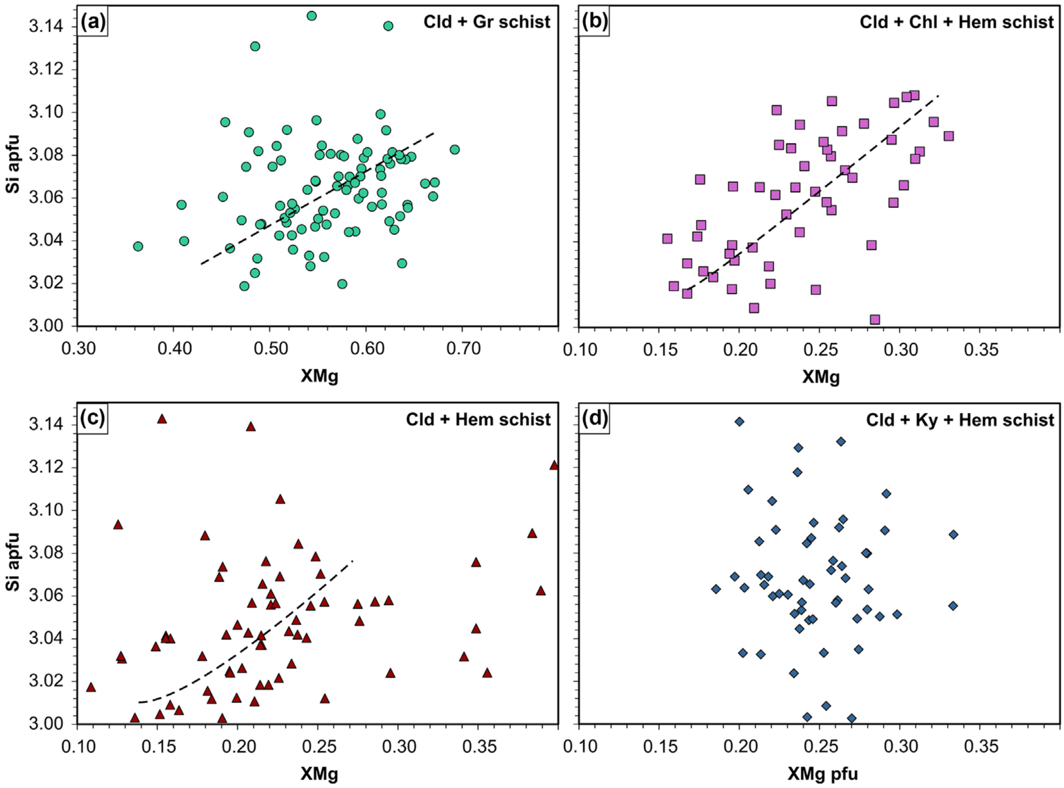

FIGURE 8 White mica chemistry (continues). (a-b-c-g) X_{Mg}–Si apfu plots for K-Na-white mica in the (a) chloritoid + graphite, (b) chloritoid + chlorite + hematite, (c) chloritoid + hematite, and (d) chloritoid + kyanite + hematite schist samples. Dashed lines highlight the best linear fit for the data points.

As a first approach, we calculated P–T-X pseudosections for $T = 400°C$, 450°C, and 500°C and P between 0.2 and 2.0 GPa. As shown in Figure 9a, where the pseudosection calculated at $T = 450°C$ is given as an example, the parageneses calculated for the measured X_{Fe2O3} (=Fe_2O_3 wt%/[FeO + Fe_2O_3 wt%]) of 0.516 indicate the presence not only of hematite, but also of kyanite as part of the mineral assemblage. Hematite and magnetite disappear from the system, regardless of P, for $X_{Fe2O3} < 0.05$. At these conditions, the predicted parageneses are: Chl–Cld–Rt at $P < 1.0$ GPa, Pg–Cld–Chl–Rt at $P = 1.0$–1.3 GPa, and Cld–Pg–Rt for $P > 1.3$ GPa (Figure 9a), which are in line with the observed assemblage of the sample (chloritoid + white mica + quartz + graphite + rutile). We obtained similar results from the P–T-X pseudosections calculated for T = 400°C and 500°C. Therefore, for phase equilibrium calculations we used an Oxygen value (O) of 0.01 wt%, consistent with low $X_{Fe2O3} < 0.05$ (Figure 9b–e). Carbon and S are not directly included in our models, but are important redox couples with iron and may affect the predicted phase assemblages. However, our predictions for low Fe_2O_3 are consistent with the stability of graphite + rutile + sulphides at high bulk fluid H/O (Connolly & Cesare, 1993).

A second issue of this sample is the overall contribution of the goethite after pyrite grains to the total Fe budget (Figure 2f). The former presence of pyrite implies that some of the FeO was fractionated as Fe in pyrite and was not available for silicates. We estimated that ~2–5% of the thin section area correspond to former pyrite. Assuming area % is equal to the volume %, goethite density of 4.0–4.2 g/cm^3, and quantitative replacement of pyrite by goethite without Fe-gain or loss by the pseudomorphs, we can estimate the actual FeO available to silicate phases to be between 3.24 and 5.25 wt%. Figure 9b–e show the pseudosections calculated for FeO = 6.07 wt% (total FeO present in the sample; Table 1), 5.5 wt%, 5.0 wt%, and 4.5 wt%, respectively. The position of the main stability fields (Pg–Cld–Rt; Pg–Cld–Chl–Rt; Chl–Cld–Rt) is roughly the same in these pseudosections. The measured X_{Mg} (0.12–0.14) of chloritoid is in equilibrium with Pg + Rt in the Cld–Pg–Rt field (the observed assemblage of the sample), only for an FeO content of ~5.0 wt% and 4.5 wt% (Figure 9d,e). The observed X_{Mg} composition of chloritoid is shifted to $T > 500°C$ in kyanite-bearing fields for FeO > 5.0 wt% (Figure 9b,c). For FeO < 4.0 wt%, chloritoid isopleths occur at unreasonably low T conditions (<300–350°C) in carpholite- and diaspore-bearing fields

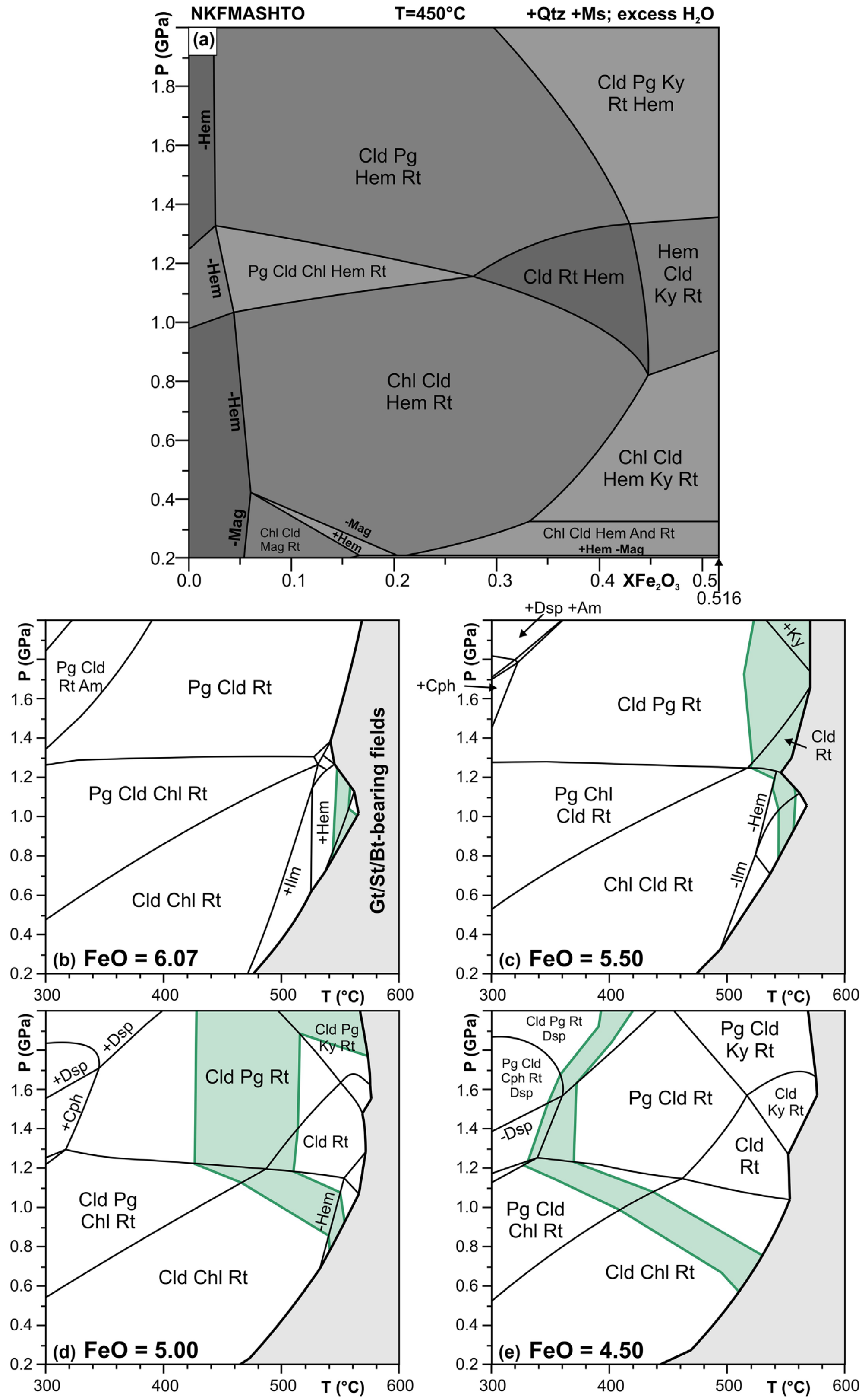

FIGURE 9 Correction of the X_{Fe2O3} and FeO content of the chloritoid + graphite schist sample. (a) P-X_{Fe2O3} pseudosection calculated at $T = 450°C$. Note the disappearance of hematite/magnetite in the system for $X_{Fe2O3} < 0.05$. (b–e) P–T pseudosections calculated for a low value of O (0.01), corresponding to X_{Fe2O3} values <0.05, for (b) FeO = 6.07 wt%, (c) FeO = 5.50 wt%, (d) FeO = 5.00 wt%, and (e) FeO = 4.50%, after the subtraction of goethitized pyrite from the system (further details in the main text). The green areas represent the area of the diagram comprised between the $X_{Mg} = 0.12$ and $X_{Mg} = 0.14$ chloritoid isopleths. Quartz and muscovite are present in all fields. Water is considered to be in excess.

that are not compatible with the mineral assemblages observed in the Massa Unit.

Therefore, we consider a value of FeO of 4.5–5.0 wt% as the best approximation for the FeO content of this sample. Figure 10 shows two P–T pseudosections calculated for 5.0 wt% and 4.5 wt% FeO, respectively. In both pseudosections, the observed chloritoid + muscovite + quartz + rutile assemblage is stable for $P > 1.2$ GPa in

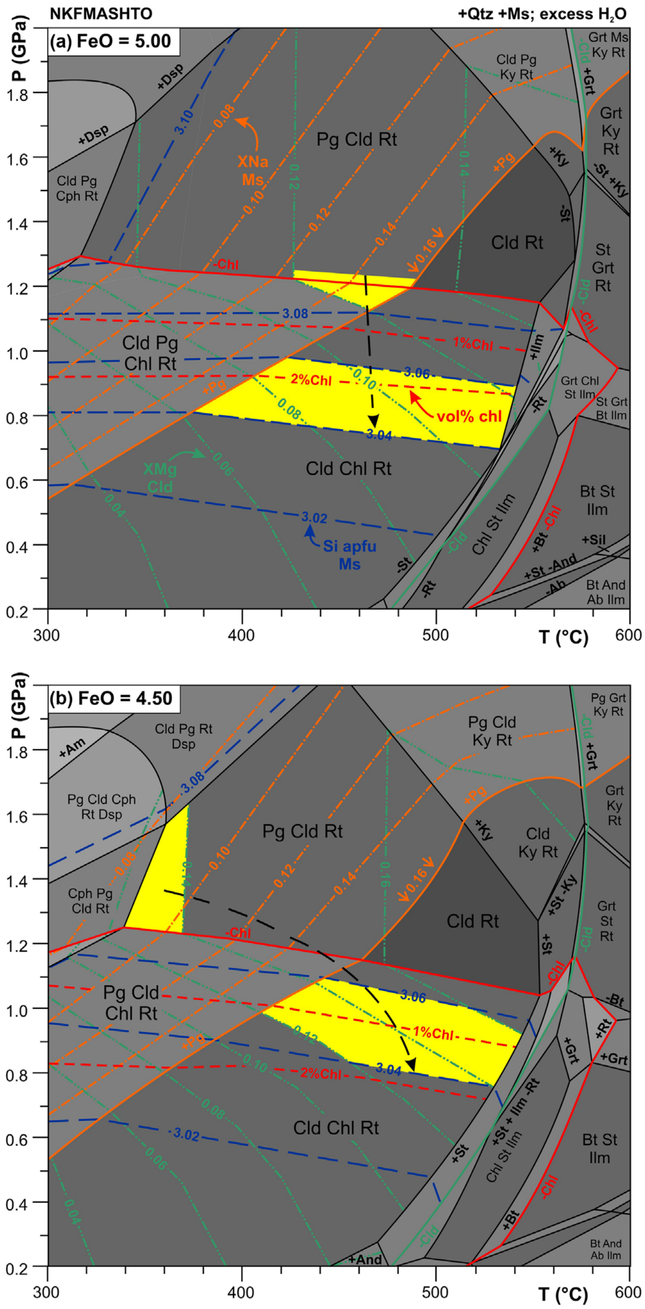

FIGURE 10 P–T pseudosections for the chloritoid + graphite schist sample assuming excess water for $T = 300–600°C$ and $P = 0.2–2.0$ GPa, calculated for (a) FeO = 5.0 wt% and (b) FeO = 4.5 wt%. Quartz and muscovite are present in all fields. Blue dashed lines: Si apfu muscovite. Orange dashed/single dotted lines: X_{Na} muscovite. Green dashed/double dotted lines: X_{Mg} chloritoid. Red dashed lines: mode (vol%) of chlorite. The yellow fields highlight the P–T conditions constrained based on chloritoid and white mica chemistry (see text for further details).

the 300–500°C range. Paragonite is part of the assemblage for $T < 480°C$, whereas at higher T paragonite is absent. At lower pressure, chlorite is stable in the Cld–Pg–Chl–Rt and Cld–Chl–Rt fields. However, the modal content of chlorite remains low (<2 vol%) down to 0.9 GPa (Figure 10).

In the sample, chlorite is present as a retrograde mineral (Figure S1) and, therefore, earlier equilibration in the Cld-Pg-Rt field followed by retrograde metamorphism either in the Cld-Pg-Chl-Rt or Cld-Chl-Rt fields is likely. Paragonite was not found in this sample. However, K-white mica analyses show a negative correlation between their X_{Na} and Si apfu contents (Figure 7a). The X_{Na} content of K-white mica (muscovite) increases with temperature, approaching the paragonite-absent Cld-Rt and Cld-Chl-Rt fields (Figure 10).

Considering first a FeO content of 5.0 wt%, the observed X_{Mg} isopleths of chloritoid (0.12–0.14) are predicted to intersect with high-Si white mica (3.08–3.09 Si apfu, $X_{Na} = 0.12–0.16$) at the boundary between the Cld-Pg-Chl-Rt and Cld-Pg-Rt fields at P = 1.1–1.3 GPa and T = 420–480°C (Figure 10a). In the paragonite-absent Cld–Chl–Rt field, low Si–white mica is stable in a wide area, as constrained by the 3.04–3.06 Si apfu muscovite isopleths, which correspond to X_{Na} compositions >0.16. This wide field corresponds to $P = 0.7–1.0$ GPa and $T = 360–520°C$ (Figure 10a). Therefore, we suggest that white mica composition likely traces an evolution from a pressure peak in which paragonite was stable to lower pressure conditions at which paragonite (absent in the sample) destabilized.

In the case of FeO = 4.5 wt%, intersection between chloritoid isopleths ($X_{Mg} = 0.12–0.14$) with white mica compositions compatible with high-Si and low-X_{Na} contents (3.06–3.08 So apfu; $X_{Na} < 0.12$) occurs at significantly lower temperatures ($T = 340–380°C$) and $P = 1.2–1.6$ GPa, mostly in the Pg-Cld-Rt field (Figure 10b). On the other hand, low-Si high-Na white mica is stable in the Cld-Chl-Rt field with $X_{Na} > 0.16$ and Si between 3.04 and 3.06 apfu. At the same P–T conditions, chloritoid is stable with $X_{Mg} = 0.12–0.16$ (Figure 10b). Intersection of these isopleths is compatible with a T peak at 0.8–1.1 GPa and 400–520°C (Figure 10b). In this case, the chloritoid composition is predicted to vary very slightly from the P to the T peak (X_{Mg} in the 0.12–0.14 range), with 0.16 X_{Mg} compositions occurring in the Cld-Chl-Rt field only for $T > 460°C$ (Figure 10b). It is interesting to note how a slight difference of ~0.5 wt% results in a large difference in the predicted P–T path from a nearly isothermal pressure decrease (Figure 10a) to a clockwise evolution from a P-peak to a T-peak (Figure 10b). In any case, we note that both phase diagrams predict a pressure peak above >1.2 GPa and a thermal peak at $P = 0.8–1.1$ GPa and $T = $ ~400–500°C.

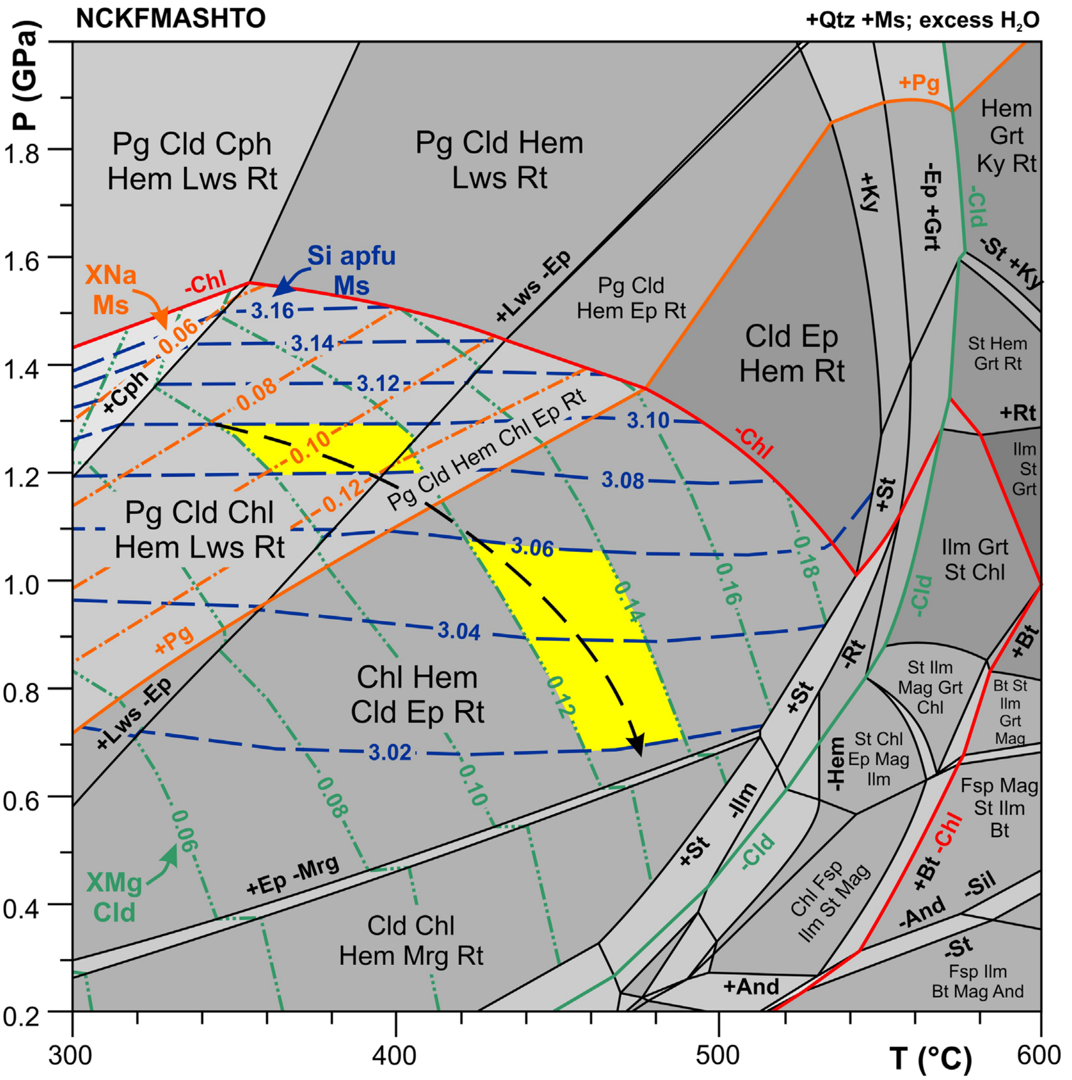

FIGURE 11 P–T pseudosection for the chloritoid + chlorite + hematite schist sample assuming excess water for $T = 300–600°C$ and $P = 0.2–2.0$ GPa. Quartz and muscovite are present in all fields. Blue dashed lines: Si apfu muscovite. Orange dashed/single dotted lines: X_{Na} muscovite. Green dashed/double dotted lines: X_{Mg} chloritoid. The yellow fields highlight the P–T conditions constrained based on chloritoid and white mica chemistry. The black dashed arrow indicates the possible P–T path. See text for a detailed explanation.

5.2 | Chloritoid + chlorite + hematite schist

The observed chloritoid + chlorite + white mica + quartz + hematite + rutile + epidote assemblage is stable across a wide P–T range between low-pressure margarite-bearing assemblages (stable at $P = 0.2–0.6$ for $T < 500°C$), and chlorite-absent fields (above $P = 1.0–1.5$ GPa) (Figure 11). In the 0.7–1.5 P range at $T < 440°C$, lawsonite is stable and epidote is not present. Paragonite occurs as an independent phase for $T < 460°C$, and it is completely replaced by white mica in the Chl-Hem-Cld-Ep-Rt field (Figure 11).

The low variance assemblages are predicted with tightly constrained mineral compositional isopleths. Comparison between predicted assemblages and compositions with those observed in the rock reveal two distinct stages of metamorphism. Indeed, chloritoid in the sample displays X_{Mg} of 0.10 (core) to 0.14 (rim) (Figure 6a), consistent with an increase in T as shown by compositional isopleths (Figure 11). The inverse correlation between Si apfu and X_{Na} in K-white mica traces an evolution from Na-poor and Si-rich (Si = 3.08–3.10 apfu at $X_{Na} = 0.10–0.12$) to Na-rich and Si-poor (Si < 3.02–3.04 apfu at $X_{Na} = 0.14–0.18$; Figure 7b) compositions. We infer that this trend indicates the former presence of paragonite in the sample that acted as a Na-storage during the growth of the early Si-rich K-white mica at HP/LT conditions, followed by replacement of paragonite by Na-rich and Si-poor K-white mica at progressively lower P and higher

T conditions. The intersection of X_{Na} white mica and chloritoid core X_{Mg} isopleths identifies early peak P metamorphism in the Pg–Cld–Chl–Hem–Lws–Rt and Pg–Cld–Hem–Chl–Ep–Rt fields between 1.2 and 1.3 GPa at T = 350–400°C. Chloritoid rim compositions (0.12–0.14 X_{Mg}) and the 3.02–3.06 Si apfu isopleths of white mica intersect at 0.7–1.1 GPa and 420–500°C, thereby identifying a lower P higher T stage of metamorphism (Figure 11). White mica is observed with compositions of $X_{Na} \sim 0.14$, consistent with those predicted in our model (Figure 11). Finally, epidote rims are observed on allanite (Figure 3d) and this is consistent with epidote growth occurring between peak P and peak T or at a later stage, possibly after the breakdown of lawsonite or other Ca-bearing phases. We, therefore, suggest that the rock reached the thermal peak of 420–500°C after an earlier pressure peak at $P > 1.2$ GPa.

5.3 | Chloritoid + hematite schist

The observed peak metamorphic assemblage is predicted in the Cld-Pg-Hem-Rt field at $P = 0.8$–1.8 GPa, and $T < 460$–480°C (Figure 12a). This field is delimited at higher pressures by the appearance of pyrophyllite, at higher temperatures by kyanite-bearing fields, and at lower pressures by the entrance of chlorite in the system (Figure 12a). In comparison with other samples, white mica analyses are scattered in the Si content, which ranges between 3.02 and 3.14 apfu, showing nearly constantly $X_{Na} = \sim 0.20$ (Figure 7g). There is a significant clustering in the range 3.02–3.08 Si apfu, which coincides with the white mica compositions predicted within this field. In particular, high-Si white mica compositions appear to be stable at lower T and low-Si compositions at higher T, respectively (Figure 12a). Similarly, chloritoid compositions are predicted to evolve within this field from $X_{Mg} < 0.12$ at $T < 340$°C to $X_{Mg} \sim 0.24$ at ~480°C, fairly in line with the observed Ctd zoning (0.16 to 0.27). We observed that the core-to-mid X_{Mg} chloritoid compositions of 0.20–0.27 (Figure 6h) are stable in a narrow T frame of 440–480°C for $P = 0.8$–1.4 GPa in the Cld Pg Hem Rt field (Figure 12a). These likely represent the peak thermal conditions reached by this sample.

The observed inverse zoning, characterized by high-Fe rims with $X_{Mg} = 0.12$–0.14 (Figure 6h), may have formed during the retrograde path through the Cld Pg Hem Chl Rt field, where decreasing values of X_{Mg} in chloritoid are predicted towards lower temperatures (Figure 12a). We do not observe chlorite in the sample, which should have formed in equilibrium with Fe-rich chloritoid during the retrograde breakdown of high-Mg chloritoid.

To better understand the development of the high-Fe rim, we calculated a tentative retrograde P–T path from $T = 480$°C to $T = 340$°C, assuming continuous fractionation of chloritoid. Figure 12b shows the modes of mineral phases expected in the sample after the fractionation of chloritoid from the system, whereas the X_{Mg} of the chloritoid grains fractionating during the retrograde P–T path is shown in the black rectangles of Figure 12a. The X_{Mg} of the chloritoid grains formed following fractionation of the Mg-rich cores are in the range of 0.12–0.16, similar to the observed values (0.13–0.14; Figure 12a). Notably, following chloritoid fractionation, the resulting rock consists largely of muscovite, paragonite, and quartz (Figure 12b), as observed. Chlorite is expected to form, but its estimated mode is <0.3 vol% (Figure 12b). Such a low modal value can be easily overlooked in the sample or be an artifact produced by uncertainties in the activity–composition models (which are not directly assessed here). Alternatively, it may represent disequilibrium in which chlorite nucleation was delayed or prohibited. In any case, the calculated low chlorite mode does not volumetrically contribute to decrease the X_{Mg} in late chloritoid rims, which we demonstrate may be driven by fractionation rather than Fe-Mg exchange with chlorite.

5.4 | Chloritoid + kyanite + hematite schist

Calculations show that this sample is always characterized by a phase that incorporates 'excess' Al_2O_3 across the entire P–T range (except in some staurolite-bearing fields): kaolinite at very low-T, pyrophyllite between 320 and 400–440°C, and kyanite at T > 400–440°C (Figure 13a). The mineral assemblage observed in this sample (kyanite + chloritoid + white mica + pyrophyllite + quartz + hematite + rutile) comprises phases that are stable in different P–T fields. In particular, pyrophyllite is stable below 400–420°C in the Cld-Prl-Hem-Rt field at P = 0.3–1.4 GPa, while kyanite is stable at T between 400 and 500°C at P = 0.3–1.7 GPa in the Cld-Hem-Ky-Rt field. Notably, we predict the presence of paragonite, which is stable at higher pressures (0.8–2.0 GPa in Figure 13a).

While the observed mineral assemblages are consistent with an early higher P stage (Pg-Hem-Cld-Prl-Rt stability field) followed by lower P thermal peak stage (Cld-Hem-Ky-Rt stability field), the predicted isopleths are not consistent with the measured mineral compositions. For example, the measured white mica compositions (Si largely between 3.04–3.10 apfu) indicate unrealistic high pressures ($P = 1.2$–2.0 GPa) when compared with the predicted compositional isopleths (Figure 7c). Such a high-pressure range is in sharp contrast with the results

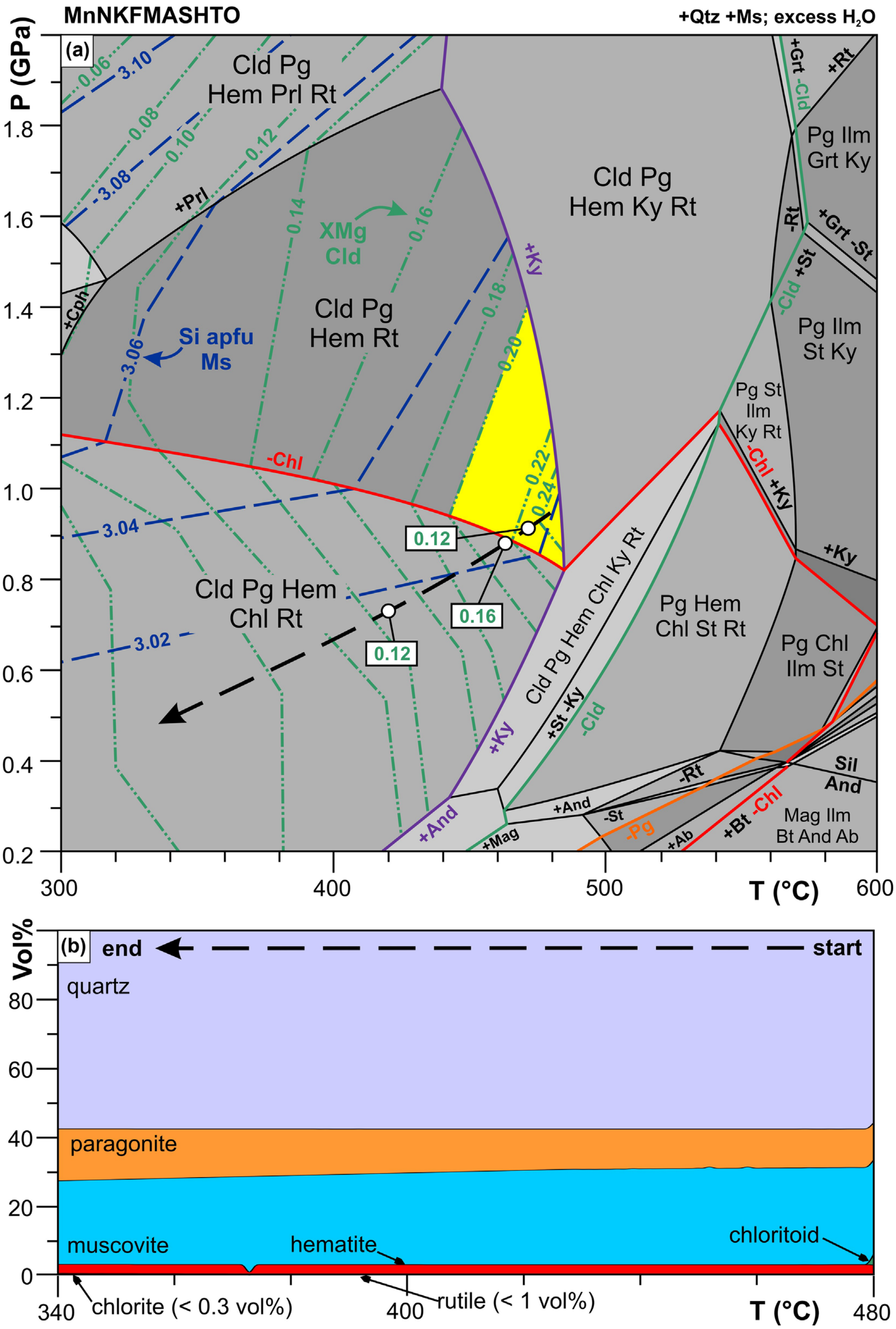

FIGURE 12 Phase equilibrium calculations for the chloritoid + hematite schist sample. (a) P-T pseudosection assuming excess water for $T = 300–600°C$ and $P = 0.2–2.0$ GPa. Quartz and muscovite are present in all fields. Blue dashed lines: Si apfu muscovite. Green dashed/double dotted lines: X_{Mg} chloritoid. The yellow fields highlight the peak P–T conditions constrained based on chloritoid chemistry (see text for further details). The black dashed arrow indicates an example retrograde P–T path to develop the observed chloritoid zoning by phase fractionation of chloritoid. The black rectangles highlight the X_{Mg} chloritoid compositions that form in the retrograde P–T path during continuous fractionation of chloritoid. (b) Mode profile for the P–T path shown in (a), calculated assuming continuous fractionation of chloritoid from the system. See text for further details.

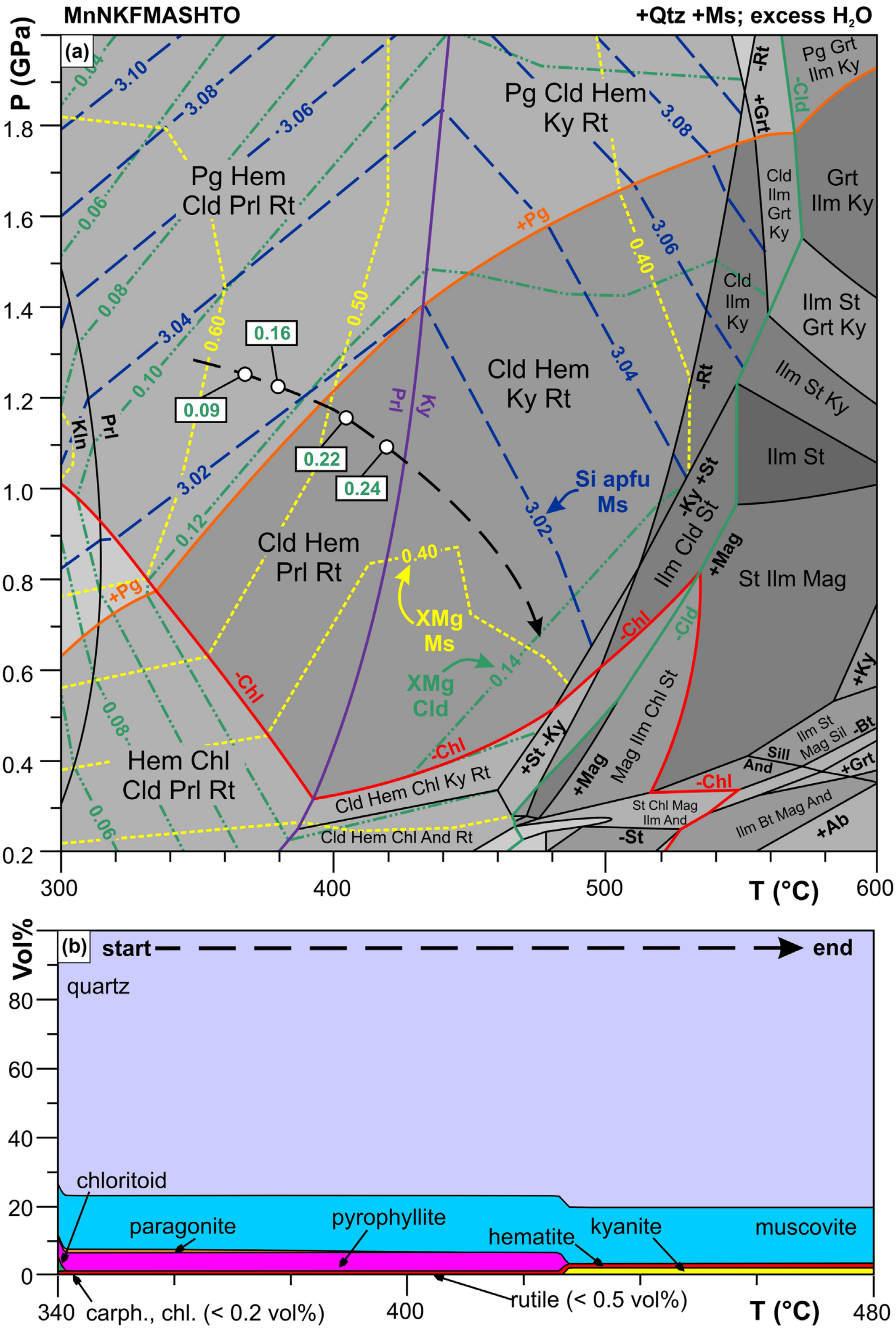

FIGURE 13 Phase equilibrium calculations for the chloritoid + kyanite + hematite schist sample. (a) P–T pseudosection calculated assuming excess water for $T = 300–600°C$ and $P = 0.2–2.0$ GPa. Quartz and muscovite are present in all fields. Blue dashed lines: Si apfu muscovite. Yellow dashed lines: X_{Mg} muscovite. Green dashed/double dotted lines: X_{Mg} chloritoid. The black dashed arrow represents the P–T path constrained on the chloritoid + chlorite + hematite sample (Figure 10). Along this P–T path, we calculated the X_{Mg} of chloritoid produced during continuous fractionation of chloritoid (X_{Mg} compositions in black rectangles). (b) Mode profile for the P–T path shown in (a), calculated assuming continuous fractionation of chloritoid from the system. See text for further details.

obtained from other samples. We also note that the observed chloritoid zoning (X_{Mg} = 0.17–0.40; Figure 6a) is not reproduced in our calculations (Figure 13a). Overall, these observations suggest that bulk rock equilibrium is not achieved. Nevertheless, the presence of paragonite, pyrophyllite, and kyanite indicates that the rock evolved from the Pg-Hem-Cld-Prl-Rt towards the Cld-Hem-Ky-Rt field, through the Cld-Hem-Prl-Rt field (Figure 13a). We consider that the unreasonably high pressure of the Pg-Cld-Hem-Ky-Rt field ($P > 1.4$ GPa) was not reached, as the P–T conditions are not consistent with those reached by other samples (e.g., Figure 11).

The observed increase in X_{Mg} of chloritoid from core to rim may be explained by continuous fractionation of chloritoid along the P–T path of the rock. To test this hypothesis, we calculated the composition of chloritoid following continuous fractionation of chloritoid from 340° at 1.3 GPa to 480°C at 0.7 GPa (dashed arrow in Figure 13a). This P–T path tested here is derived from the one estimated for the chloritoid + chlorite + hematite sample (Figure 11). The mineral modes predicted over the chloritoid fractionation path are shown in Figure 13b: After fractionation of an earlier high-Fe chloritoid (X_{Mg} = 0.09–0.16), the later chloritoid that forms in the system becomes increasingly Mg-rich up to values of X_{Mg} = 0.22–0.24, crystallizing at ~400°C. Along this P–T path, pyrophyllite, making up 8 vol% of the sample at low T, disappears to produce quartz and 4 vol% kyanite at T = 420°C.

Even assuming chloritoid fractionation, there is still a large gap between the predicted (0.09–0.24) and observed (>0.4) X_{Mg}, although phase fractionation appears to be a suitable process to produce zoning from Fe-rich to Mg-rich compositions. This mismatch can be explained by considering (1) the very limited Mg content of the sample (0.13 wt%; Table 1), (2) the adopted white mica model [Mica(W)], and (3) the fractionation of chloritoid. Indeed, such a low bulk Mg must be very sensitive to uncertainties in the Mg, Fe partitioning among silicates calculated by solution models and the measure of bulk rock chemistry by whole rock fusion. In particular, we observe that the predicted white mica composition incorporates less Fe + Mg apfu compared to white mica compositions analyzed in the sample: this consequently lowers the predicted X_{Mg} of chloritoid, considering the high FeO content of the rock. An additional issue is that pyrophyllite and paragonite coexist as metastable phases in the sample, indicating that the reactive bulk composition at peak T conditions is not equal to the measured bulk composition. Regardless, the predicted trend is consistent with those of other samples, and it is evident that a combination of chloritoid fractionating and decreasing-*P* increasing-*T* from peak *P* conditions can produce the observed chloritoid + hematite + kyanite + white mica + rutile assemblage at peak *T*.

6 | DISCUSSION

6.1 | P–T conditions of metamorphism

The investigated samples from the Massa Unit record development of chloritoid grains progressively richer in Mg, associated with a concomitant transition from Si-rich Na-poor to Si-poor Na-rich K-white micas (Figures 5–8). This evolution is consistent with pressure decrease and temperature increase during metamorphism. Indeed, the increase of X_{Mg} in chloritoid, albeit complicated by fractionation and the presence of Fe_2O_3, indicates an increase in metamorphic temperature (Vidal et al., 1999), whereas the Si-content of K-white mica is known to increase with pressure (Massonne & Schreyer, 1987; Massonne & Szpurka, 1997). Paragonite tends to be stable at higher pressure (Guidotti et al., 1994) and, consequently, the progressive enrichment in Na in Si-poor micas is consistent with pressure decrease during the destabilization of paragonite, which is present only as a relict phase in most of the samples (Figures 2g and 5f).

Relics of the M1 pressure peak are best preserved in the chloritoid + graphite and the chloritoid + chlorite + hematite samples, consistent with our thermodynamic modelling (Figures 10a,b and 11). Both samples recorded peak metamorphic pressures of 1.1–1.3 GPa at temperatures of 350–400°C (Figures 10b and 11). However, the uncertainties in the bulk FeO content of the chloritoid + graphite sample, due to the subtraction of the Fe contributed by goethitized pyrite, propagates to significant systematic errors on the X_{Mg} of chloritoid (Figure 9). Consequently, we obtained two very different P–T paths for this sample when considering either FeO = 5.0 or 4.5 wt% in the bulk composition (Figure 10a,b). Nevertheless, the P–T path reconstructed for FeO = 4.5 wt% (Figure 10b) predicts reasonably well the observed compositions of chloritoid and white mica and the stable mineral assemblages, and overlaps with the P–T path as reconstructed for the chloritoid + chlorite + hematite sample (Figure 11), therefore representing the likely P–T path experienced by this rock. Moreover, the assemblage Pg-Hem-Cld-Prl-Rt predicted for the chloritoid + kyanite + hematite sample is consistent with occurrence of relict paragonite and pyrophyllite in this sample, suggesting peak *P* conditions >0.8 GPa at $T < 440$°C. However, differences in the X_{Mg} contents of white mica and chloritoid from the observed compositions preclude a precise P–T determination. Consequently, we consider the P–T estimates of 1.2–1.3 GPa at 350–400°C, as constrained by the low variance assemblage Pg-Cld-Chl-Hem-Lws-Rt, for the chloritoid + chlorite + hematite sample as the best estimate for peak pressure M1 metamorphism (Figure 11). The predicted peak T conditions are consistent across the four studied samples (Figure 10–13). Again, the low variance assemblage and closely spaced isopleths for the chloritoid + chlorite + hematite sample constrains the peak thermal conditions to 0.7–1.1 GPa and 420–480°C. While other samples predict phase equilibria consistent with the observed assemblages and the P–T range calculated from the chloritoid + chlorite + hematite sample, the calculated P–T windows are rather large. For example, the chloritoid + graphite sample has a large uncertainty on the estimated temperature (380–520°C; Figure 10), due to a high variance Cld-Chl-Rt assemblage with widely spaced isopleths, whereas the large uncertainties in P (0.8–1.4 GPa) for the chloritoid + hematite sample result from subparallel isopleths for X_{Mg} in chloritoid and Si in muscovite, respectively (Figure 12a). Finally, the prograde transition from pyrophyllite to kyanite in the chloritoid + kyanite + hematite sample indicates a peak *T* of >400°C (Figure 13). However, while the peak assemblage is consistent with the observations, the X_{Mg} of Cld is not well predicted (see Section 5.4). Generally, the observed trend to lower Si and higher Na in K-white mica composition associated with the X_{Mg} increase as observed in the studied samples, is consistent with a *T* increase during decompression. Consequently, the *P* decrease and *T* increase to conditions of 0.7–1.1 GPa and 420–480°C, as constrained by modelling of the chloritoid + chlorite + hematite sample (Figure 11) and the chloritoid + graphite sample for FeO = 4.5 wt% (Figure 10b), represent our best estimate for the metamorphic climax in the Massa Units. A clockwise metamorphic P–T path is therefore reconstructed for the Massa Unit at the metamorphic peak, characterized by a pressure loop from a P peak (1.2–1.3 GPa at 350–400°C) to a T peak (07–1.1 GPa at 440–480°C) at lower pressure conditions (Figure 15).

6.2 | Effect of the Fe_2O_3 content on chloritoid- and kyanite-bearing assemblages

Kyanite is often used as a key petrogenetic indicator in Al-bearing metapelites, since its appearance in regional metamorphic successions generally indicates a change in metamorphic grade or metamorphic conditions during peak burial. Here we show that the presence or absence of kyanite in the Massa unit is not primarily controlled by a change in metamorphic conditions but depends instead on the high bulk rock Fe_2O_3 and FeO fractionation operated by growth of chloritoid during prograde metamorphism.

Metapelites are often modelled assuming all Fe to be divalent, an assumption that may not be justified in many cases. Most of the samples investigated in this work contain hematite as part of the metamorphic assemblage and the bulk rock $Fe^{3+}/\Sigma Fe$ value is higher than zero. In addition to oxide phases, Fe^{3+} can also partition into silicate minerals. The compilation of Forshaw and Pattison (2021) shows that white mica, on average, can contain ~0.17 ± 0.13 Fe^{3+} apfu (on 22 O basis), while chlorite may incorporate 0.31 ± 0.27 Fe^{3+} apfu (on 28 O basis), on average.

In this study we estimate by charge balance that the Fe^{3+} contents in chloritoid is up to 0.08–0.10 apfu on 12 O basis (online repository). The $Fe^{3+}/\Sigma Fe$ contents of natural chloritoid tend to be low (Deer et al., 1992), consistent with the low Fe^{3+} in chloritoid predicted in our models. Instead, at elevated Fe^{3+} contents in metapelitic rocks, in which the silicate phases are effectively saturated in Fe^{3+}, ferric iron partitions strongly into oxide minerals, namely hematite-ilmenite solid solution and magnetite. Consequently, despite typically having low Mg contents, metapelites may produce minerals with high X_{Mg} at very elevated $Fe^{3+}/\Sigma Fe$ because little Fe^{2+} is available for silicate phases.

If the bulk rock Fe is mainly sequestered in oxides as Fe^{3+}, the modes of Fe-Al silicates, like chloritoid, chlorite, or mica, are suppressed. As a result, Al and Si are available to form Al_2SiO_5 phases at *T* conditions lower than in less oxidized metapelitic rocks. The development of Al-silicates and high X_{Mg} chloritoid at Fe_2O_3-rich conditions can be visualized through P–T-X pseudosections calculated for X_{Fe2O3} (=Fe_2O_3 wt%/[FeO wt% + Fe_2O_3 wt %]) ratios between 0 and 1.

In Figure 14, we show a series of such P–T-X pseudosections for the investigated samples, calculated at T = 450°C and assuming H_2O-saturated conditions. In all cases, kyanite is stabilized in the system towards high X_{Fe2O3} values in which hematite is stable, as observed in our samples. For example, in the chloritoid + kyanite + hematite schist, kyanite is stabilized at $X_{Fe2O3} > 0.25$, well below the measured X_{Fe2O3} of 0.56 (Figure 14a). While kyanite is not present in the chloritoid + hematite and chloritoid + chlorite + hematite schists, it is noteworthy that both samples have measured X_{Fe2O3} values of 0.73 and 0.34, respectively, producing conditions which are close to, but just below, the X_{Fe2O3} required for appearance of kyanite in the system (~0.75–0.80 and 0.4, respectively; Figure 14b,c).

At higher X_{Fe2O3} (>0.8–0.9), chloritoid is unstable relative to chlorite ± carpholite, which exhibit very high

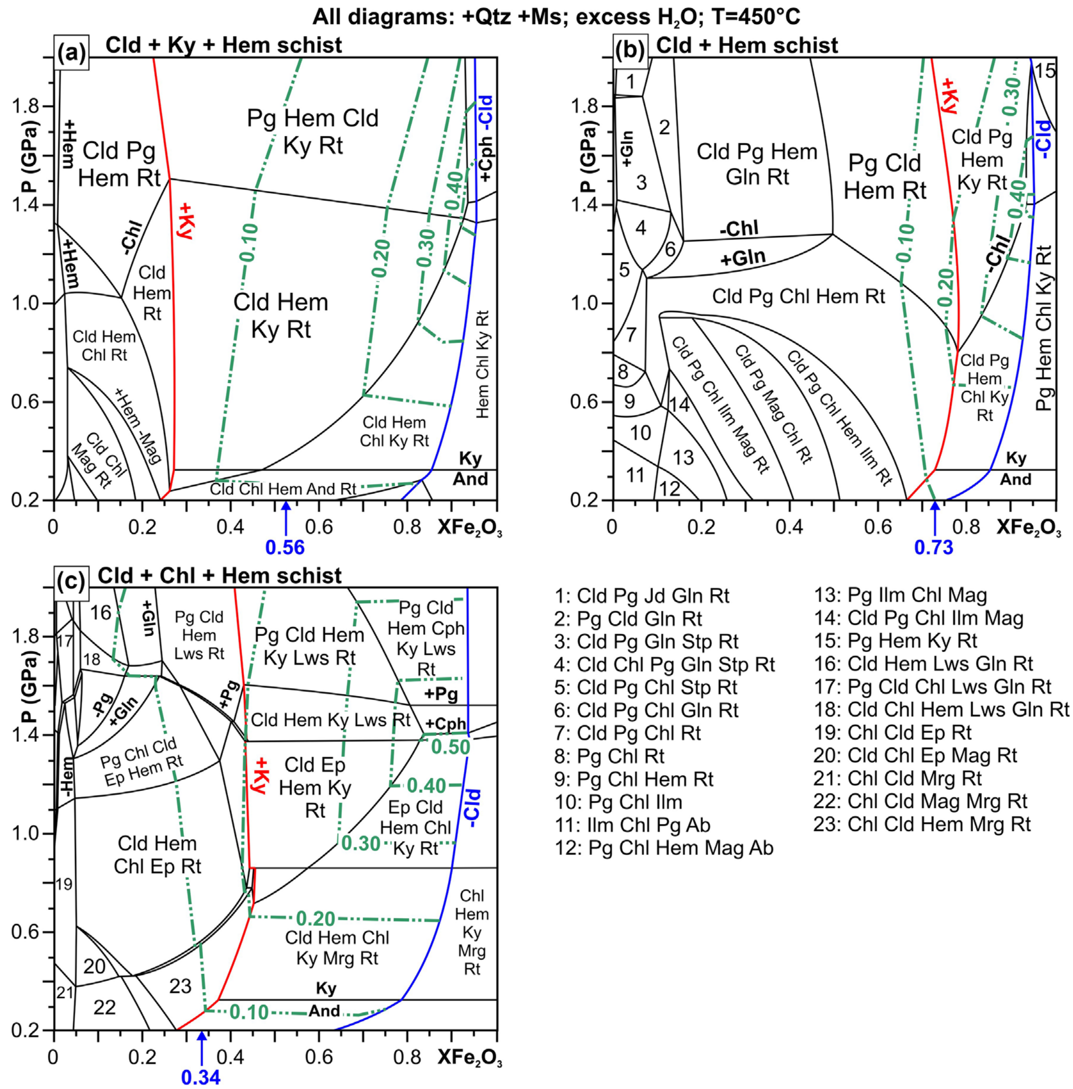

FIGURE 14 P-X_{Fe2O3} diagrams calculated assuming excess water at $T = 450°C$ for $X_{Fe2O3} = 0–1$ and $P = 0.2–2.0$ GPa in (a) the chloritoid + kyanite + hematite, (b) the chloritoid + hematite, and (c) the chloritoid + chlorite + hematite schist samples. Quartz and muscovite are present in all fields. The blue value on the X_{Fe2O3} axis is the measured X_{Fe2O3} for the sample. The green dashed/double dotted lines mark the calculated X_{Mg} composition of chloritoid. See discussion.

X_{Mg} under these conditions (Figure 14). The P–T conditions at which chloritoid is unstable occur at X_{Fe2O3} values only slightly higher than those measured for some samples (e.g., $X_{Fe2O3} = 0.73$ in the chloritoid + hematite schist) and, therefore, it is possible that these conditions might occur in nature. Finally, all calculations show that high values of bulk X_{Fe2O3} correspond to higher values of X_{Mg} in chloritoid (Figure 14). In general, X_{Mg} in chloritoid increases with X_{Fe2O3}, reaching values as high as $X_{Mg} > 0.40$. This is consistent with the observations from our samples, where the chloritoid with the highest X_{Mg} values chiefly occurs in hematite-bearing samples with elevated X_{Fe2O3} (Figures 5 and 6a and Table 1). The X_{Mg} in chloritoid is also strongly dependent on the pressure (e.g. note the P-related variations in Figure 14) and temperature (e.g., X_{Mg} of chloritoid in Figure 12a) of metamorphism at high X_{Fe2O3}, with the direct consequence that the X_{Mg} is expected to vary greatly.

Consequently, chloritoid is anticipated to develop strongly zoned profiles as a function of the P–T path in high X_{Fe2O3} rocks. Consistent with this prediction, we observe strongly zoned chloritoid grains in the oxidized chloritoid + kyanite + hematite ($X_{Fe2O3} = 0.54$; Figures 6a and 14a) and chloritoid + hematite ($X_{Fe2O3} = 0.73$; Figures 6a and 14b) samples, but not in the more reduced chloritoid + graphite + pyrite sample (chloritoid $X_{Mg} = 0.10–0.14$). In the high X_{Fe2O3} samples, the decrease in P and increase in T along the predicted P–T path favours fractionation of the early Fe-rich core to produce progressively more exotic Mg-rich rims.

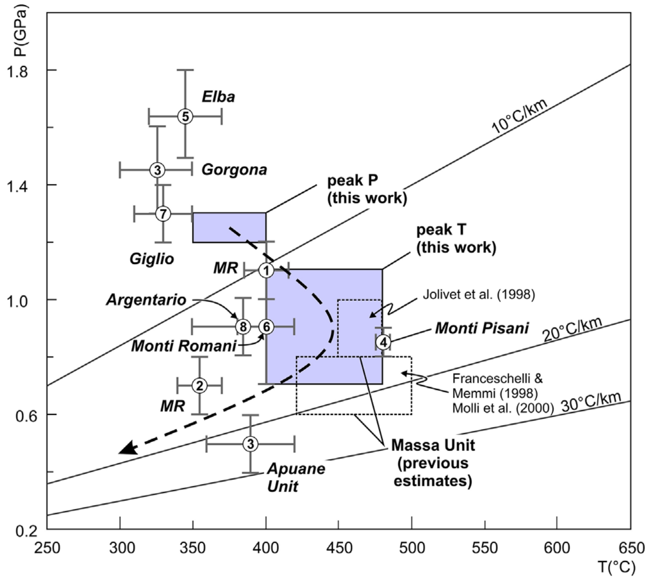

FIGURE 15 Summary diagram showing the P–T results of the present work (light blue rectangles) compared with previous estimates from the Massa Unit (black dashed rectangles), the Apuane unit, and the Northern Apennines. The pressure peak estimated in the present work for the Massa unit is consistent with similar estimates from Southern Tuscany (Giglio, Elba, Monticiano–Roccastrada), whereas our estimated temperature peak is comparable with previous estimates from the Massa Unit. The dashed arrow highlights the proposed P–T path of the Massa Unit. MR: Monticiano Roccastrada. References: 1. Brogi & Giorgetti (2012); 2. Giorgetti et al. (1998); 3. Jolivet et al. (1998), Rossetti et al. (2001); 4. Lo Pò and Braga (2014); 5. Papeschi et al. (2020); 6. Papeschi et al. (2020), 7. Rossetti et al. (1999), Giuntoli & Viola (2021); 8. Theye et al. (1997).

6.3 | Geological implications

Over the past decades, several petrological studies have been carried out on the chloritoid-bearing rocks from the Apuane Alps (Apuane and Massa units) and P–T constraints have been obtained based on the X_{Mg} in chloritoid, the application of the chloritoid-chlorite geothermometer of Vidal et al. (1999), and petrological considerations on the position of chloritoid-forming reactions in the KFMASH system (Franceschelli et al., 1996, 1997; Jolivet et al., 1998; Franceschelli & Memmi, 1999; Molli, Giorgetti, & Meccheri, 2000; Molli et al., 2002). Collectively, these studies have indicated metamorphic conditions of 0.6–1.0 GPa at 420–500°C for the Massa Unit and of 0.4–0.6 GPa at 350–450°C for the Apuane Unit (Figure 15). These thermo-barometric estimates place the Apuane region apart from the rest of the TMUs of the Northern Apennines, where higher pressures ($P = 1.0$–1.8 GPa) have been reported at similar, if not lower, metamorphic temperatures (300–450°C; Theye et al., 1997; Jolivet et al., 1998; Giorgetti et al., 1998; Papeschi et al., 2020; Papeschi, Pontesilli, et al., 2022; Rossetti et al., 1999; Vignaroli et al., 2009; Figure 15).

Our results, based on phase equilibrium modelling of chloritoid-bearing metapelites, show that the peak metamorphic pressures reached by the Massa Unit have been underestimated, as the unit reached at least pressures of 1.2–1.3 GPa at 350–480°C (Figure 15). Our temperature estimates are in line with previous studies and with recent estimates obtained by RSCM thermometry (485 ± 28°C; Molli, Brovarone, et al., 2018). However, we were able to discriminate an early pressure peak of 1.2–1.3 GPa at 350–400°C from a later thermal peak of 440–480°C at 0.7–1.1 GPa (Figure 15). Based on these new thermobaric estimates, if we assume an average crustal density of 2700 kg/m^3, the Massa Unit reached a burial depth of at least 45 km under a geothermal gradient <10°C/km, a gradient significantly colder than the previous estimates of ∼20–30°C/km (Molli, Brovarone, et al., 2018; Molli, Carlini, et al., 2018; Montomoli et al., 2001), but fully compatible with a subduction environment (Ernst, 1973; Syracuse et al., 2010) and the palaeo-geothermal conditions as estimated for the HP–LT units exposed in the hinterland of the Northern Apennines (Theye et al., 1997; Giorgetti et al., 1998; Jolivet et al., 1998; Rossetti et al., 1999, 2001; Papeschi et al., 2020; Ryan et al., 2021). If we extrapolate the burial conditions as regulated by the cold palaeogeothermal geothermal gradient as estimated for the Massa unit to the Apuane Unit, considering the temperature peak of 397 ± 64°C as obtained via RSCM thermometry by Molli, Brovarone, et al. (2018), we can infer higher peak metamorphic pressures of at least 1.0 GPa. Similarly, if the same assumptions are made for the burial history of the Tuscan Nappe, burial depth of ∼25 km were reached at T ∼230–270°C (Molli, Brovarone, et al., 2018; Montomoli et al., 2001).

The thermobaric evolution, as reconstructed in this study, highlights that the thermal peak was reached after the peak pressure was attained in the Massa Unit. This evidence, indicates that the D1/M1 fabric of the Massa Unit is composite (see also Molli, Giorgetti, & Meccheri, 2000) and records moderate heating from ∼10 to ∼20°C/km during the switch from peak burial to exhumation at depth in the orogenic roots of the Northern Apennine orogenic wedge. Significantly, this is the first example of such P–T evolution documented in the HP/LT metamorphic units of the Northern Apennines (Figure 15). However, the diffuse preservation of low-T peak assemblages in the hinterland of the Northern Apennine chain ((Fe–Mg)–carpholite in metapelites and lawsonite in metabasites; Theye et al., 1997; Giorgetti et al., 1998; Jolivet et al., 1998; Rossetti et al., 2001; Brogi & Giorgetti, 2012; Bianco et al., 2019; Giuntoli & Viola, 2021) document that exhumation of the orogenic roots dominantly occurred during convergence and nappe stacking (Carosi et al., 2004; Molli, Giorgetti, & Meccheri, 2000; Rossetti et al., 1999, 2002; Ryan et al., 2021). We then speculate that this peculiar P–T evolution at peak metamorphic conditions might be the signal of the thermal relaxation caused by the continuous (slow) underthrusting at depth of the continental material and consequent crustal thickening (England & Thompson, 1984; Goffè et al., 2003; Weller et al., 2013) during the growth of the Apennine orogenic wedge.

7 | CONCLUSIONS

The chloritoid schists of the Massa Unit represent a unique natural laboratory to constrain the development of chloritoid-bearing assemblages at varying $FeO–Fe_2O_3$ contents (oxidizing and reducing conditions) at low-grade metamorphic conditions. Three main conclusions that can be drawn from this study:

(1) The Fe_2O_3 content plays a major role not only in governing the composition of mineral phases, like the X_{Mg} in chloritoid, but it is also responsible for the formation of Al-silicates such as pyrophyllite and kyanite.
(2) Neglecting ferric iron in low-grade metapelites may lead to erroneous inferences when estimating the P–T conditions of deformation based exclusively on the X_{Mg} content in ferromagnesian minerals, since Fe_2O_3 is normally (mostly) stored in oxide minerals, making the resulting 'effective' bulk rock composition enriched in Mg, even in Mg-poor rocks like metapelites.
(3) Fe_2O_3 enhances the variability of X_{Mg} as function of P–T space, exacerbating the effects of chloritoid fractionation during prograde and retrograde metamorphism.

Finally, the results of this study allow the P–T conditions of metamorphism in the Massa Unit to be refined and to recognize for the first time an earlier pressure peak at 350–400°C and 1.2–1.3 GPa, which was followed by a thermal peak at 440–480°C and 0.7–1.1 GPa.

These results indicate that peak metamorphism in the continental-derived units of the Alpi Apuane was achieved under (1) a cold palaeo-gradient conditions, typical of subduction zone metamorphism (<10°C/km), followed by (2) moderate heating (up to 480°C) during decompression at high-pressure conditions, which occured during the deep underthrusting of the Adria continental crust to form the Northern Apennine orogen.

ACKNOWLEDGEMENTS

The research presented here was carried out during the COVID–19 pandemic, only thanks to the support to the fieldwork of S. Papeschi by his wife, Carlotta Papeschi, and his granny, Lina Bargagna. We are also grateful to Prof. Giovanni Musumeci for discussion during this study. We also thank Eleonora Braschi and Andrea Orlando for their assistance with the microprobe. We would like to thank Dr. Clare Warren for editorial handling and two anonymous reviewers for their constructive comments that greatly improved the original manuscript. Open Access funding enabled and organized by Projekt DEAL.

DATA AVAILABILITY STATEMENT

The data that support the findings of this study are openly available in data.Mendeley.com at https://data.mendeley.com/datasets/wm3nwkrd4m, reference number DOI: 10.17632/wm3nwkrd4m.1.

ORCID

Samuele Papeschi https://orcid.org/0000-0002-5774-7119
Federico Rossetti https://orcid.org/0000-0001-8071-7252
Jesse B. Walters https://orcid.org/0000-0002-1275-8826

REFERENCES

Albee, A. L. (1972). Metamorphism of pelitic schists: Reaction relations of chloritoid and staurolite. *Geological Society of America Bulletin*, *83*(11), 3249–3268. https://doi.org/10.1130/0016-7606(1972)83[3249:MOPSRR]2.0.CO;2

Ashworth, J. R., & Evirgen, M. M. (1984). Mineral chemistry of regional chloritoid assemblages in the chlorite zone, Lycian nappes, south-West Turkey. *Mineralogical Magazine*, *48*(347), 159–165. https://doi.org/10.1180/minmag.1984.048.347.01

Azañón, J. M., & Goffé, B. (1997). Ferro-and magnesiocarpholite assemblages as record of high-P, low-T metamorphism in the central Alpujarrides, Betic cordillera (SE Spain). *European Journal of Mineralogy-Ohne Beihefte*, *9*(5), 1035–1052. https://doi.org/10.1127/ejm/9/5/1035

Baldacci, F., Elter, P., Giannini, E., Giglia, G., Lazzarotto, A., Nardi, R., & Tongiorgi, M. (1967). Nuove osservazioni sul problema della Falda Toscana e sulla interpretazione dei flysch arenacei tipo "Macigno" dell'Appennino settentrionale. *Memorie Della Societa Geologica Italiana*, *6*(2), 213–244.

Balen, D., Horváth, P., Finger, F., & Starijaš, B. (2013). Phase equilibrium, geothermobarometric and xenotime age dating constraints on the Alpine metamorphism recorded in chloritoid schists from the southern part of the Tisia mega-unit (Slavonian Mts., NE Croatia). *International Journal of Earth Sciences*, *102*(4), 1091–1109. https://doi.org/10.1007/s00531-012-0850-8

Bianco, C., Godard, G., Halton, A., Brogi, A., Liotta, D., & Caggianelli, A. (2019). The lawsonite-glaucophane blueschists of Elba Island (Italy). *Lithos*, *348*, 105198. https://doi.org/10.1016/j.lithos.2019.105198

Boccaletti, M., Elter, P., & Guazzone, G. (1971). Plate tectonic models for the development of the Western Alps and Northern Apennines. *Nature Physical Science*, *234*(49), 108–111. https://doi.org/10.1038/physci234108a0

Bonini, M., Sani, F., Stucchi, E. M., Moratti, G., Benvenuti, M., Menanno, G., & Tanini, C. (2014). Late Miocene shortening of the Northern Apennines back-arc. *Journal of Geodynamics*, *74*, 1–31. https://doi.org/10.1016/j.jog.2013.11.002

Bouybaouene, M. L., Goffé, B., & Michard, A. (1995). High-pressure, low-temperature metamorphism in the Sebtides nappes, Northern Rif, Morocco. *Geogaceta*, *17*, 117–119.

Brogi, A., & Giorgetti, G. (2012). Tectono–metamorphic evolution of the siliciclastic units in the Middle Tuscan Range (inner Northern Apennines): Mg–carpholite bearing quartz veins related to syn–metamorphic syn–orogenic foliation. *Tectonophysics*, *526–529*, 167–184. https://doi.org/10.1016/j.tecto.2011.09.015

Brunet, C., Monié, P., Jolivet, L., & Cadet, J. P. (2000). Migration of compression and extension in the Tyrrhenian Sea, insights from $^{40}Ar/^{39}Ar$ ages on micas along a transect from Corsica to Tuscany. *Tectonophysics*, *321*(1), 127–155. https://doi.org/10.1016/S0040-1951(00)00067-6

Carmignani, L., & Kligfield, R. (1990). Crustal extension in the Northern Apennines: The transition from compression to extension in the Alpi Apuane core complex. *Tectonics*, *9*(6), 1275–1303. https://doi.org/10.1029/TC009i006p01275

Carmignani, L., Decandia, F. A., Disperati, L., Fantozzi, P. L., Kligfield, R., Lazzarotto, A., Liotta, D., & Meccheri, M. (2001). Inner Northern Apennines. In G. B. Vai & I. P. Martini (Eds.), *Anatomy of an Orogen: The Apennines and adjacent Mediterranean basins* (pp. 197–214). Kluwer Academic Publishers.

Carmignani, L., Conti, P., Cornamusini, G., Meccheri, M., & Crescenti, U. (2004). The internal Northern Apennines, the Northern Tyrrhenian Sea and the Sardinia-Corsica block. *Geology of Italy. Special Volume, Italian Geological Society, IGC*, *32*, 59–77.

Carminati, E., Lustrino, M., & Doglioni, C. (2012). Geodynamic evolution of the central and western Mediterranean: Tectonics vs. igneous petrology constraints. *Tectonophysics*, *579*, 173–192. https://doi.org/10.1016/j.tecto.2012.01.026

Carosi, R., Leoni, L., Montomoli, C., & Sartori, F. (2003). Very low-grade metamorphism in the Tuscan nappe, Northern Apennines, Italy: Relationships between deformation and metamorphic indicators in the La Spezia mega-fold. *Swiss Bulletin of Mineralogy and Petrology*, *83*(1), 15–32.

Carosi, R., Montomoli, C., & Pertusati, P. C. (2004). Late tectonic evolution of the Northern Apennines: The role of contractional tectonics in the exhumation of the Tuscan units. *Geodinamica Acta*, *17*(4), 253–273. https://doi.org/10.3166/ga.17.253-273

Cassinis, G., Perotti, C., & Santi, G. (2018). Post-Variscan Verrucano-like deposits in Italy, and the onset of the alpine tectono-sedimentary cycle. *Earth-Science Reviews*, *185*, 476–497. https://doi.org/10.1016/j.earscirev.2018.06.021

Cerrina Feroni, A., Plesi, G., Fanelli, G., Leoni, L., & Martinelli, P. (1983). Contributo alla conoscenza dei processi metamorfici di grado molto basso (anchimetamorfismo) a carnico della falda toscana nell'area del ricoprimento apuano. *Bollettino Della Societa Geologica Italiana*, *102*(2–3), 269–280.

Chopin, C. (1983). Magnesiochloritoid, a key-mineral for the petrogenesis of high-grade pelitic blueschists. *Bulletin de Mineralogie*, *106*(6), 715–717. https://doi.org/10.3406/bulmi.1983.7692

Chopin, C., & Schreyer, W. (1983). Magnesiocarpholite and magnesiochloritoid: Two index minerals of pelitic blueschists and their preliminary phase relations in the model system MgO–Al_2O_3–SiO_2–H_2O. *American Journal of Science*, *283*, 72–96.

Chopin, C., Seidel, E., Theye, T., Ferraris, G., Ivaldi, G., & Catti, M. (1992). Magnesiochloritoid, and the Fe-mg series in the chloritoid group. *European Journal of Mineralogy*, *4*, 67–76. https://doi.org/10.1127/ejm/4/1/0067

Ciarapica, G., & Passeri, L. (1994). The Tuscan nappe in Northern Apennines: Data, doubts, hypotheses. *Memorie Della Societa Geologica Italiana*, *48*(1), 7–22.

Connolly, J. A. (2005). Computation of phase equilibria by linear programming: A tool for geodynamic modeling and its application to subduction zone decarbonation. *Earth and Planetary Science Letters*, *236*(1–2), 524–541. https://doi.org/10.1016/j.epsl.2005.04.033

Connolly, J. A. D. (2009). The geodynamic equation of state: What and how. *Geochemistry, Geophysics, Geosystems*, *10*(10), n/a. https://doi.org/10.1029/2009GC002540

Connolly, J. A. D., & Cesare, B. (1993). C–O–H–S fluid composition and oxygen fugacity in graphitic metapelites. *Journal of Metamorphic Geology*, *11*(3), 379–388. https://doi.org/10.1111/j.1525-1314.1993.tb00155.x

Conti, P., Pisa, A. D., Gattiglio, M., & Meccheri, M. (1993). The pre-alpine basement in the Alpi apuane (Northern Apennines, Italy). In *Pre-Mesozoic geology in the Alps* (pp. 609–621). Springer. https://doi.org/10.1007/978-3-642-84640-3_36

Conti, P., Carmignani, L., Massa, G., Meccheri, M., Patacca, E., Scandone, P., & Pieruccioni, D. (2019). *Note illustrative alla carta geologica d'Italia scala 1:50000. Foglio 249. Massa Carrara*. Servizio Geologico d'Italia, Istituto Superiore per la Protezione e la Ricerca Ambientale.

Conti, P., Cornamusini, G., & Carmignani, L. (2020). An outline of the geology of the Northern Apennines (Italy), with geological map at 1: 250,000 scale. *Italian Journal of Geosciences*, *139*(2), 149–194. https://doi.org/10.3301/IJG.2019.25

Coward, M., & Dietrich, D. (1989). Alpine tectonics—An overview. *Geological Society, London, Special Publications*, *45*(1), 1–29. https://doi.org/10.1144/GSL.SP.1989.045.01.01

Deer, W., Howie, R. A., & Zussman, J. (1992). *An introduction to the rock-forming minerals*. Longman.

Di Pisa, A., Franceschelli, M., Leoni, L., & Meccheri, M. (1985). Regional variation of the metamorphic temperatures across the Tuscanid I unit and its implications on the Alpine metamorphism (Apuan Alps, Northern Tuscany). *Neues Jahrbuch für Mineralogie (Abhandlungen)*, *151*(2), 197–211.

Di Vincenzo, G., Godard, G., & Molli, G. (2022). Dating low-grade deformation: Role of lithology and strain partitioning on Ar isotope Records in the Alpi Apuane of Northern Apennines (Italy). *Tectonics*, *41*(7), e2022TC007248.

Droop, G. T. R. (1987). A general equation for estimating Fe^{3+} concentrations in ferromagnesian silicates and oxides from microprobe analyses, using stoichiometric criteria. *Mineralogical Magazine*, *51*(361), 431–435. https://doi.org/10.1180/minmag.1987.051.361.10

Elter, P. (1975). Introduction à la géologie de l'Apennin septentrional. *Bulletin de la Société géologique de France*, *7*(6), 956–962. https://doi.org/10.2113/gssgfbull.S7-XVII.6.956

England, P. C., & Thompson, A. B. (1984). Pressure—Temperature—Time paths of regional metamorphism I. heat transfer during the evolution of regions of thickened continental crust. *Journal of Petrology*, *25*(4), 894–928. https://doi.org/10.1093/petrology/25.4.894

Ernst, W. G. (1973). Blueschist metamorphism and P–T regimes in active subduction zones. *Tectonophysics*, *17*(3), 255–272. https://doi.org/10.1016/0040-1951(73)90006-1

Faccenna, C., Becker, T. W., Lucente, F. P., Jolivet, L., & Rossetti, F. (2001). History of subduction and back arc extension in the Central Mediterranean. *Geophysical Journal International*, *145*(3), 809–820. https://doi.org/10.1046/j.0956-540x.2001.01435.x

Fellin, M. G., Reiners, P. W., Brandon, M. T., Wüthrich, E., Balestrieri, M. L., & Molli, G. (2007). Thermochronologic evidence for the exhumational history of the Alpi Apuane metamorphic core complex, Northern Apennines, Italy. *Tectonics*, *26*(6), n/a. https://doi.org/10.1029/2006TC002085

Forshaw, J. B., & Pattison, D. R. (2021). Ferrous/ferric (Fe^{2+}/Fe^{3+}) partitioning among silicates in metapelites. *Contributions to Mineralogy and Petrology*, *176*(9), 1, 63–26. https://doi.org/10.1007/s00410-021-01814-4

Franceschelli, M., & Memmi, I. (1999). Zoning of chloritoid from kyanite-facies metapsammites, Alpi Apuane, Italy. *Mineralogical Magazine*, *63*(1), 105–110. https://doi.org/10.1180/002646199548222

Franceschelli, M., Leoni, L., Memmi, I., & Puxeddu, M. (1986). Regional distribution of Al-silicates and metamorphic zonation in the low-grade Verrucano metasediments from the Northern Apennines, Italy. *Journal of Metamorphic Geology*, *4*(3), 309–321. https://doi.org/10.1111/j.1525-1314.1986.tb00353.x

Franceschelli, M., Puxeddu, M., Carcangiu, G., Gattiglio, M., & Pannuti, F. (1996). Breccia-hosted manganese-rich minerals of Alpi Apuane, Italy: A marine, redox-generated deposit. *Lithos*, *37*(4), 309–333. https://doi.org/10.1016/0024-4937(95)00026-7

Franceschelli, M., Memmi, I., Carcangiu, G., & Gianelli, G. (1997). *Prograde and retrograde chloritoid zoning in low temperature metamorphism*. Alpi Apuane.

Fuhrman, M. L., & Lindsley, D. H. (1988). Ternary-feldspar modeling and thermometry. *American Mineralogist*, *73*(3–4), 201–215.

Ganguly, J. (1969). Chloritoid stability and related paragenesis; theory, experiments, and applications. *American Journal of Science*, *267*(8), 910–944. https://doi.org/10.2475/ajs.267.8.910

Guidotti, C. V., Sassi, F. P., Blencoe, J. G., & Selverstone, J. (1994). The paragonite-muscovite solvus: I. P-T-X limits derived from the Na-K compositions of natural, quasibinary paragonite-muscovite pairs. *Geochimica et Cosmochimica Acta*, *58*(10), 2269–2275.

Giorgetti, G., Goffe, B., Memmi, I., & Nieto, F. (1998). Metamorphic evolution of Verrucano metasediments in Northern Apennines; new petrological constraints. *European Journal of Mineralogy*, *10*(6), 1295–1308. https://doi.org/10.1127/ejm/10/6/1295

Giuntoli, F., & Viola, G. (2021). Cyclic brittle-ductile oscillations recorded in exhumed high-pressure continental units: A record of deep episodic tremor and slow slip events in the Northern Apennines. *Geochemistry, Geophysics, Geosystems*, *22*(9), e2021GC009805.

Goffé, B., Bousquet, R., Henry, P., & Le Pichon, X. (2003). Effect of the chemical composition of the crust on the metamorphic evolution of orogenic wedges. *Journal of Metamorphic Geology*, *21*(2), 123–141. https://doi.org/10.1046/j.1525-1314.2003.00422.x

Holland, T. J. B., & Powell, R. (2011). An improved and extended internally consistent thermodynamic dataset for phases of petrological interest, involving a new equation of state for solids. *Journal of Metamorphic Geology*, *29*(3), 333–383. https://doi.org/10.1111/j.1525-1314.2010.00923.x

Hoschek, G. (1969). The stability of staurolite and chloritoid and their significance in metamorphism of pelitic rocks. *Contributions to Mineralogy and Petrology*, *22*(3), 208–232. https://doi.org/10.1007/BF00387954

Jolivet, L., Faccenna, C., Goffé, B., Mattei, M., Rossetti, F., Brunet, C., Storti, F., Funiciello, R., Cadet, J. P., d'Agostino, N., & Parra, T. (1998). Midcrustal shear zones in postorogenic extension: Example from the Northern Tyrrhenian Sea. *Journal of Geophysical Research - Solid Earth*, *103*(B6), 12123–12160. https://doi.org/10.1029/97JB03616

Kligfield, R. (1979). The Northern Apennines as a collisional orogen. *American Journal of Science*, *279*(6), 676–691. https://doi.org/10.2475/ajs.279.6.676

Kligfield, R., Hunziker, J., Dallmeyer, R. D., & Schamel, S. (1986). Dating of deformation phases using K-Ar and $^{40}Ar/^{39}Ar$ techniques: Results from the Northern Apennines. *Journal of Structural Geology*, *8*(7), 781–798. https://doi.org/10.1016/0191-8141(86)90025-8

López-Carmona, A., Pitra, P., & Abati, J. (2013). Blueschist-facies metapelites from the Malpica–Tui unit (NW Iberian massif): Phase equilibria modelling and H_2O and Fe_2O_3 influence in high-pressure assemblages. *Journal of Metamorphic Geology*, *31*(3), 263–280. https://doi.org/10.1111/jmg.12018

Lo Pò, D., & Braga, R. (2014). Influence of ferric iron on phase equilibria in greenschist facies assemblages: The hematite-rich metasedimentary rocks from the Monti Pisani (Northern Apennines). *Journal of Metamorphic Geology*, *32*(4), 371–387. https://doi.org/10.1111/jmg.12076

Massonne, H. J., & Schreyer, W. (1987). Phengite geobarometry based on the limiting assemblage with K-feldspar, phlogopite, and quartz. *Contributions to Mineralogy and Petrology*, *96*(2), 212–224. https://doi.org/10.1007/BF00375235

Massonne, H. J., & Szpurka, Z. (1997). Thermodynamic properties of white micas on the basis of high-pressure experiments in the systems $K_2O–MgO–Al_2O_3–SiO_2–H_2O$ and $K_2O–FeO–Al_2O_3–SiO_2–H_2O$. *Lithos*, *41*(1–3), 229–250. https://doi.org/10.1016/S0024-4937(97)82014-2

Massonne, H. J., & Willner, A. P. (2008). Phase relations and dehydration behaviour of psammopelite and mid-ocean ridge basalt at very-low-grade to low-grade metamorphic conditions. *European Journal of Mineralogy*, *20*(5), 867–879. https://doi.org/10.1127/0935-1221/2008/0020-1871

Molli, G. (2008). Northern Apennine–Corsica orogenic system: An updated overview. *Geological Society, London, Special Publications*, *298*(1), 413–442. https://doi.org/10.1144/SP298.19

Molli, G., Giorgetti, G., & Meccheri, M. (2000). Structural and petrological constraints on the tectono-metamorphic evolution of the Massa unit (Alpi Apuane, NW Tuscany, Italy). *Geological Journal*, *35*(3–4), 251–264. https://doi.org/10.1002/gj.860

Molli, G., Conti, P., Giorgetti, G., Meccheri, M., & Oesterling, N. (2000). Microfabric study on the deformational and thermal history of the Alpi Apuane marbles (Carrara marbles), Italy. *Journal of Structural Geology*, *22*(11–12), 1809–1825. https://doi.org/10.1016/S0191-8141(00)00086-9

Molli, G., Giorgetti, G., & Meccheri, M. (2002). Tectono-metamorphic evolution of the Alpi Apuane metamorphic complex: New data and constraints for geodynamic model. *Bollettino Della Societa Geologica Italiana*, *1*(2), 789–800.

Molli, G., Carlini, M., Vescovi, P., Artoni, A., Balsamo, F., Camurri, F., Clemenzi, L., Storti, F., & Torelli, L. (2018). Neogene 3-D structural architecture of the North-West Apennines: The role of the low-angle normal faults and basement thrusts. *Tectonics*, *37*(7), 2165–2196. https://doi.org/10.1029/2018TC005057

Molli, G., Brovarone, A. V., Beyssac, O., & Cinquini, I. (2018). RSCM thermometry in the Alpi Apuane (NW Tuscany, Italy): New constraints for the metamorphic and tectonic history of the inner Northern Apennines. *Journal of Structural Geology*, *113*, 200–216. https://doi.org/10.1016/j.jsg.2018.05.020

Montomoli, C., Ruggieri, G., Boiron, M. C., & Cathelineau, M. (2001). Pressure fluctuation during uplift of the Northern Apennines (Italy): A fluid inclusions study. *Tectonophysics*, *341*(1–4), 121–139. https://doi.org/10.1016/S0040-1951(01)00197-4

Nerone, S., Groppo, C., & Rolfo, F. (2023). Equilibrium and kinetic approaches to understand the occurrence of the uncommon chloritoid + biotite assemblage. *European Journal of Mineralogy*, *35*(2), 305–320. https://doi.org/10.5194/ejm-35-305-2023

Papeschi, S., Musumeci, G., Massonne, H. J., Mazzarini, F., Ryan, E. J., & Viola, G. (2020). High-P (P= 1.5–1.8 GPa) blueschist from Elba: Implications for underthrusting and exhumation of continental units in the Northern Apennines. *Journal of Metamorphic Geology*, *38*(5), 495–525. https://doi.org/10.1111/jmg.12530

Papeschi, S., Pontesilli, A., Romano, C., Rossetti, F., & Theye, T. (2022). Alpine subduction zone metamorphism in the Palaeozoic successions of the Monti Romani (northern Apennines, Italy). *Journal of Metamorphic Geology*, *40*, 919–953. https://doi.org/10.1111/jmg.12650

Papeschi, S., Vannucchi, P., Hirose, T., & Okazaki, K. (2022). Deformation and material transfer in a fossil subduction channel: Evidence from the island of Elba (Italy). *Tectonics*, *41*(7), e2021TC007164.

Patacca, E., Scandone, P., & Meccheri, M. (2011). Stratigraphic and structural revision of the Massa "Schuppenzone" (Alpi Apuane, Northern Apennines). *Rendiconti Online Della Società Geologica Italiana*, *15*, 102–105.

Patacca, E., Scandone, P., Conti, P., Mancini, S., & Massa, G. (2013). Ligurian-derived olistostrome in the Pseudomacigno formation of the Stazzema zone (Alpi Apuane, Italy). Geological implications at regional scale. *Italian Journal of Geosciences*, *132*(3), 463–476. https://doi.org/10.3301/IJG.2013.05

Pourteau, A., Bousquet, R., Vidal, O., Plunder, A., Duesterhoeft, E., Candan, O., & Oberhänsli, R. (2014). Multistage growth of Fe–mg–carpholite and Fe–mg–chloritoid, from field evidence to thermodynamic modelling. *Contributions to Mineralogy and Petrology*, *168*(6), 1, 1090–25. https://doi.org/10.1007/s00410-014-1090-7

Reutter, K. J., Teichmuller, M., Teichmuller, R., & Zanaucchi, G. (1978). Coalification studies in the Northern Apeninnes and paleogeothermal implications. In H. Closs, D. Roeder, & K. Schmidt (Eds.), *Alps, Apennines and Hellenides* (pp. 261–267). Schweizerbartsche Verlagbuchhandlung.

Ricci Lucchi, F. (1986). The Oligocene to recent foreland basins of the Northern Apennines. In P. A. Allen & P. Homewood (Eds.), *Foreland Basins*, 103–139. https://doi.org/10.1002/9781444303810.ch6

Rossetti, F., Faccenna, C., Jolivet, L., Funiciello, R., Tecce, F., & Brunet, C. (1999). Syn-versus post-orogenic extension: The case study of Giglio Island (Northern Tyrrhenian Sea, Italy). *Tectonophysics*, *304*(1–2), 71–93. https://doi.org/10.1016/S0040-1951(98)00304-7

Rossetti, F., Faccenna, C., Jolivet, L., Funiciello, R., Goffé, B., Tecce, F., … Vidal, O. (2001). Structural signature and exhumation PTt path of the Gorgona blueschist sequence (Tuscan archipelago, Italy). *Ofioliti*, *26*(2a), 175–186.

Rossetti, F., Faccenna, C., Jolivet, L., Goffé, B., & Funiciello, R. (2002). Structural signature and exhumation P-T-t paths of the blueschist units exposed in the interior of the Northern Apennine chain, tectonic implications. *Bollettino Della Societa Geologica Italiana*, *121*(1), 829–842.

Rossetti, F., Cavazza, W., Di Vincenzo, G., Lucci, F., & Theye, T. (2023). Alpine tectono-metamorphic evolution of the Corsica basement. *Journal of Metamorphic Geology*, *41*(2), 299–326. https://doi.org/10.1111/jmg.12696

Ryan, E., Papeschi, S., Viola, G., Musumeci, G., Mazzarini, F., Torgersen, E., Sørensen, B. E., & Ganerød, M. (2021). Syn-orogenic exhumation of high-P units by upward extrusion in an accretionary wedge: Insights from the Eastern Elba nappe stack (Northern Apennines, Italy). *Tectonics*, *40*(5), e2020TC006348.

Schumacher, J. C. (1991). Empirical ferric iron corrections: Necessity, assumptions, and effects on selected geothermobarometers. *Mineralogical Magazine*, *55*(378), 3–18. https://doi.org/10.1180/minmag.1991.055.378.02

Siivola, J., & Schmid, R. (2007). List of mineral abbreviations. Recommendations by the IUGS Subcommission on the Systematics of Metamorphic Rocks. In D. Fettes & J. Desmons (Eds.), *Metamorphic rocks: A classification and glossary of terms. Recommendations of the International Union of Geological Sciences Subcommission on the systematics of metamorphic rocks*. Cambridge University Press.

Simon, G., Chopin, C., & Schenk, V. (1997). Near-end-member magnesiochloritoid in prograde-zoned pyrope, Dora-Maira massif, Western Alps. *Lithos*, *41*(1–3), 37–57. https://doi.org/10.1016/S0024-4937(97)82004-X

Spear, F. S., & Pattison, D. R. (2017). The implications of overstepping for metamorphic assemblage diagrams (MADs). *Chemical Geology*, *457*, 38–46. https://doi.org/10.1016/j.chemgeo.2017.03.011

Syracuse, E. M., van Keken, P. E., & Abers, G. A. (2010). The global range of subduction zone thermal models. *Physics of the Earth and Planetary Interiors*, *183*(1–2), 73–90. https://doi.org/10.1016/j.pepi.2010.02.004

Theye, T., Seidel, E., & Vidal, O. (1992). Carpholite, sudoite, and chloritoid in low-grade high-pressure metapelites from Crete and the Peloponnese, Greece. *European Journal of Mineralogy*, *4*, 487–508. https://doi.org/10.1127/ejm/4/3/0487

Theye, T., Reinhardt, J., Goffe, B., Jolivet, L., & Brunet, C. (1997). Ferro-and magnesiocarpholite from the Monte Argentario (Italy): First evidence for high-pressure metamorphism of the metasedimentary Verrucano sequence, and significance for PT path reconstruction. *European Journal of Mineralogy*, *9*, 859–874. https://doi.org/10.1127/ejm/9/4/0859

Vidal, O., Theye, T., & Chopin, C. (1994). Experimental study of chloritoid stability at high pressure and various fO2 conditions. *Contributions to Mineralogy and Petrology*, *118*(3), 256–270. https://doi.org/10.1007/BF00306647

Vidal, O., Goffé, B., Bousquet, R., & Parra, T. (1999). Calibration and testing of an empirical chloritoid chlorite mg-Fe exchange thermometer and thermodynamic data for daphnite. *Journal of Metamorphic Geology*, *17*, 25–40. https://doi.org/10.1046/j.1525-1314.1999.00174.x

Vignaroli, G., Faccenna, C., Jolivet, L., Piromallo, C., & Rossetti, F. (2008). Subduction polarity reversal at the junction between the Western Alps and the Northern Apennines, Italy. *Tectonophysics*, *450*(1–4), 34–50. https://doi.org/10.1016/j.tecto.2007.12.012

Vignaroli, G., Faccenna, C., Rossetti, F., & Jolivet, L. (2009). Insights from the Apennines metamorphic complexes and their bearing on the kinematics evolution of the orogen. *Geological Society, London, Special Publications*, *311*(1), 235–256. https://doi.org/10.1144/SP311.9

Walters, J. B. (2022). MinPlot: A mineral formula recalculation and plotting program for electron probe microanalysis. *Mineralogia*, *53*(1), 51–66. https://doi.org/10.2478/mipo-2022-0005

Weller, O. M., St-Onge, M. R., Waters, D. J., Rayner, N., Searle, M. P., Chung, S. L., Palin, R. M., Lee, Y. H., & Xu, X. (2013). Quantifying Barrovian metamorphism in the Danba structural culmination of Eastern Tibet. *Journal of Metamorphic Geology*, *31*(9), 909–935. https://doi.org/10.1111/jmg.12050

White, R. W., Powell, R., Holland, T. J. B., & Worley, B. A. (2000). The effect of TiO_2 and Fe_2O_3 on metapelitic assemblages at greenschist and amphibolite facies conditions: Mineral equilibria calculations in the system K_2O-FeO-MgO-Al_2O_3-SiO_2-H_2O-TiO_2-Fe_2O_3. *Journal of Metamorphic Geology*, *18*(5), 497–511. https://doi.org/10.1046/j.1525-1314.2000.00269.x

White, R. W., Powell, R., & Clarke, G. L. (2002). The interpretation of reaction textures in Fe-rich metapelitic granulites of the Musgrave block, Central Australia: Constraints from mineral equilibria calculations in the system K_2O–FeO–MgO–Al_2O_3–SiO_2–H_2O–TiO_2–Fe_2O_3. *Journal of Metamorphic Geology*, *20*(1), 41–55. https://doi.org/10.1046/j.0263-4929.2001.00349.x

White, R. W., Powell, R., Holland, T. J. B., Johnson, T. E., & Green, E. C. R. (2014). New mineral activity–composition relations for thermodynamic calculations in metapelitic systems. *Journal of Metamorphic Geology*, *32*(3), 261–286. https://doi.org/10.1111/jmg.12071

Zhou, T., Dong, C., & Phillips, G. N. (1994). Chemographic analysis of assemblages involving pyrophyllite, chloritoid, chlorite, kaolinite, kyanite, quartz: Application to metapelites in the Witwatersrand goldfields, South Africa. *Journal of Metamorphic Geology*, *12*(5), 655–666. https://doi.org/10.1111/j.1525-1314.1994.tb00049.x

SUPPORTING INFORMATION

Additional supporting information can be found online in the Supporting Information section at the end of this article.

Table S1. List of the investigated samples. The mineral assemblage is shown in modal order. Mineral abbreviations after Siivola and Schmid (2007).

Figure S1. Masses of chlorite (deep Berlin blue colours, mostly at the center of the image) in the chloritoid + graphite schist sample. These are often present as masses or as pseudomorphs over chloritoid, indicating that they formed as an alteration or retrograde product. Field of view: 3 mm.

How to cite this article: Papeschi, S., Rossetti, F., & Walters, J. B. (2023). Growth of kyanite and Fe-Mg chloritoid in Fe_2O_3-rich high-pressure–low-temperature metapelites and metapsammites: A case study from the Massa Unit (Alpi Apuane, Italy). *Journal of Metamorphic Geology*, *41*(8), 1049–1079. https://doi.org/10.1111/jmg.12736

APPENDIX A. METHODS

Electron microprobe analyses (point analyses and Wavelength Dispersive Spectrometer X-ray maps) were carried out at CNR-ICG (Firenze, Italy) using a JEOL JXA-8230 equipped with five spectrometers and multiple analytical crystals. Analytical conditions for point analyses were 15 kV accelerating voltage and variable beam current (5 nA for phyllosilicates, 20 nA for oxides, kyanite, and chloritoid). Counting times were 15 s on peak and 7 s on background for major elements except Na, for which 10 and 5 s respectively were used. Minor elements counting times were: 30–40 s on peak and 15–20s on background. The analytical standards were biotite MAC, chamosite MAC, hornblende Kak, Kaersutite AST (Astimex), Augite Kak, Pyrite Kak, Diopside AST, Titanite MAC, Ilmenite Smith, and Rutile AST. We analysed: Structural formulae of the analysed minerals were recalculated based on 11 oxygens for white mica, 14 for chlorite, 12 for chloritoid, 5 for kyanite, 2 for quartz, 3 for hematite, and 2 for rutile. White mica, chlorite, and chloritoid compositions were calculated using MinPlot (Walters, 2022). The Fe^{3+} content was recalculated based on charge balancing for chloritoid assuming a cation sum of 8 (Droop, 1987; Schumacher, 1991) and we considered all Fe in kyanite to be trivalent (Deer et al., 1992). For chlorite and white mica, for which the estimation of Fe^{3+} based on charge balancing is not possible, we assumed all iron to be divalent. Representative mineral analyses are provided in Tables 2 and 3. Concentration maps for major elements were also produced by continuous stepwise movements of the thin section under the electron beam at 15 kV accelerating voltage, 50 nA beam current, and 100 ms dwell time.

The major (Si, Ti, Al, Fe, Mn, Mg, Ca, Na, K, P) and trace element composition of the samples and their loss on ignition (LOI) was determined by Lithium Metaborate/Tetraborate Fusion ICP and ICP-MS, the FeO and Fe_2O_3 content was measured by QOP (fluorine) wet chemical titration at Activation Laboratories Ltd. (Ancaster, Ontario, Canada).